UNCLASSIFIED MASTER COPY FOR REPRODUCTION PURPOSES

AD-A218 776

REPORT DOCUMENTATION PAGE

1a. REPORT SECURITY CLASSIFICATION: Unclassified	1b. RESTRICTIVE MARKINGS
2a. SECURITY CLASSIFICATION AUTHORITY	3. DISTRIBUTION/AVAILABILITY OF REPORT: Approved for public release; distribution unlimited.
2b. DECLASSIFICATION/DOWNGRADING SCHEDULE	
4. PERFORMING ORGANIZATION REPORT NUMBER(S)	5. MONITORING ORGANIZATION REPORT NUMBER(S): ARO 23617.13-MS
6a. NAME OF PERFORMING ORGANIZATION: Univ of Wisconsin-Madison; 6b. OFFICE SYMBOL (If applicable)	7a. NAME OF MONITORING ORGANIZATION: U. S. Army Research Office
6c. ADDRESS (City, State, and ZIP Code): Madison, WI 53706	7b. ADDRESS (City, State, and ZIP Code): P. O. Box 12211, Research Triangle Park, NC 27709-2211
8a. NAME OF FUNDING/SPONSORING ORGANIZATION: U. S. Army Research Office; 8b. OFFICE SYMBOL (If applicable)	9. PROCUREMENT INSTRUMENT IDENTIFICATION NUMBER: DAAL03-86-K-0114
8c. ADDRESS (City, State, and ZIP Code): P. O. Box 12211, Research Triangle Park, NC 27709-2211	10. SOURCE OF FUNDING NUMBERS: PROGRAM ELEMENT NO. / PROJECT NO. / TASK NO. / WORK UNIT ACCESSION NO

11. TITLE (Include Security Classification)

Solidification of Highly Undercooled Liquid Droplets

12. PERSONAL AUTHOR(S)

J. H. Perepezko

13a. TYPE OF REPORT	13b. TIME COVERED	14. DATE OF REPORT (Year, Month, Day)	15. PAGE COUNT
Final	FROM 7/1/86 TO 6/30/89	Jan 1990	74

16. SUPPLEMENTARY NOTATION

The view, opinions and/or findings contained in this report are those of the author(s) and should not be construed as an official Department of the Army position, policy, or decision, unless so designated by other documentation.

17. COSATI CODES		
FIELD	GROUP	SUB-GROUP

18. SUBJECT TERMS (Continue on reverse if necessary and identify by block number)

Crystallization, Metals, Liquid Metals, Undercooling, Solidification, Recalescence, External Cooling, Droplet Emulsion Technique

19. ABSTRACT (Continue on reverse if necessary and identify by block number)

Research has been focused upon metastable phase formation and the controlling phase selection reactions, the evolution of solidification microstructure under the combined influence of undercooling, recalescence and external cooling and several other aspects of undercooled alloy solidification and product structure stability. The experimental approach that has been applied to carry out these studies is based on the droplet emulsion technique. With this method, samples may be produced which exhibit large undercoolings prior to solidification during slow cooling (10-30°C/min) and which may be maintained in the metastable undercooled state for extended time periods without the intervention of crystallization.

20. DISTRIBUTION/AVAILABILITY OF ABSTRACT: ☐ UNCLASSIFIED/UNLIMITED ☐ SAME AS RPT. ☐ DTIC USERS	21. ABSTRACT SECURITY CLASSIFICATION: Unclassified
22a. NAME OF RESPONSIBLE INDIVIDUAL	22b. TELEPHONE (Include Area Code) / 22c. OFFICE SYMBOL

DD FORM 1473, 84 MAR 83 APR edition may be used until exhausted. All other editions are obsolete.

SECURITY CLASSIFICATION OF THIS PAGE

UNCLASSIFIED

INTRODUCTION

The undercooling of liquid metals below their equilibrium melting point is a common occurrence in solidification. Throughout the analysis of solidification processing, the conditions of nucleation and liquid undercooling behavior have been recognized for the strong influence that they can exert on the initial stage of solidification structure formation. Moreover, undercooling phenomenon are recognized as being of central importance in the nucleation of equilibrium and non-equilibrium crystalline phases and in the formation of amorphous phases. At the same time, in theoretical and applied crystal growth work the amount of liquid undercooling is regarded as one of the critical parameters in determining the path of morphological evolution and the final solidification structure.

Although undercooling effects can be observed during the slow cooling of a liquid metal, most often, before an appreciable undercooling can develop, crystallization initiates at some heterogeneous catalytic site (1). In practice, nucleation catalysts may be activated by any of a number of different types of sites in contact with the liquid including impurity aggregates, foreign inclusions and container walls. However, a number of experimental approaches have been developed which are effective in extending the range of observable undercooling and in permitting the examination of the rapid crystallization that develops following nucleation at high undercooling.

The most commonly used methods for generating high liquid undercoolings prior to solidification involve a rapid quenching from the melt. Indeed, the main attention in rapid solidification processing (RSP) methods has been focused upon the attainment of high cooling rates in the range of 10^4 to 10^8 °C/sec. With these methods small liquid volumes are quenched either by contact with a substrate as in melt spinning and directed energy beam processing or in an inert gas as in atomization. However, the most important impact of RSP can be related directly to the solidification structures and the new opportunities for structure control by innovative alloy

design and processing strategies. The wide range of reported microstructure variations encompass not only equilibrium phase mixtures with refined microstructural scale, but also novel microstructures such as supersaturated solid solutions, metastable intermediate phases and amorphous solids. While the development of refined microstructures during RSP can be viewed in terms of the decrease in local solidification time and the growth features of the principal microstructural components (2) the understanding of novel microstructures representing non-equilibrium phases requires a consideration of the level of undercooling at the onset of nucleation in addition to rapid growth kinetics (3). In fact, the available free energy for non-equilibrium phase formation is directly related to the amount of undercooling. With increasing levels of undercooling the product phase selection involved in nucleation can be expanded to involve an increased variety (3,4) and to allow competitive growth kinetics to play an important role in the evolution of different microstructural morphologies (5).

The establishment of melt undercooling as a key variable in microstructural development provides an important link between rapid quenching studies and undercooling research. Indeed, in many respects undercooling is a more fundamental parameter than cooling rate. In most work on RSP, cooling rate is used as a convenient process variable. However, in solidification studies on undercooled samples, it has been demonstrated that undercooling can be treated in a meaningful way as a process variable (3,6-9). Accordingly, examination of solidification in undercooled liquids can contribute to the basic understanding necessary for a successful microstructure control and alloy design in the optimization of RSP treatments.

While progress has been made, there are still important challenges to understanding that remain to be addressed in the solidification of highly undercooled liquids. For example, the reliable prediction of nucleation control of structure selection is an open issue, but there are developments in experiment and analysis that offer promise for new predictive capability. Although the experience in rapid solidification has increased, it is certainly not a mature area. New advances continue to be made. Some developments represent totally new observations and others represent a better understanding of reported behavior. Beyond the potential for innovative

applications, rapid solidification has provided an experimental vehicle and a stimulus that has pushed the limits of the basic understanding of structure development. These developments have a wide impact on a range of processing applications including spray deposition, surface melting and composite fabrication.

I. BACKGROUND

I.A Droplet-emulsion Undercooling Technique

A large continuous sample of liquid metal contains a variety of catalytic nucleation centers which acts to preclude the attainment of high levels of undercooling prior to solidification. Since crystallization will be catalyzed by the most potent nucleation site present, a means of circumventing the effect of catalytic sites such as oxides or container walls is necessary in order to observe extensive undercooling. Following from this basis, an effective approach to obtain large undercoolings is to disperse the bulk liquid into a collection of fine droplets which effectively isolates potent nucleation sites into a small fraction of the droplet population. The effect of these catalytic sites will then be restricted to the few drops in which they are located. The high purity liquid sample is dispersed within a suitable carrier fluid, and droplet independence is maintained by the formation of thin, inert surface coatings which are not catalytic to crystallization. When a sample of liquid metal in the form of a stabilized droplet emulsion is cooled, those drops containing potent nucleants will freeze at low undercoolings, but the majority will not freeze until reaching the maximum nucleation undercooling level which can range from 0.3 to 0.4 T_m (10).

The experience gained from earlier work on relatively low melting point metals ($T_m < 500$ °C) using organic carrier fluids has recently permitted the extension of the droplet emulsion technique to high melting point metals (6,11). With the current experience it is now possible to prepare droplet emulsion samples in molten salt fluids from alloys with melting points up to 1100 °C (including Cu-base alloys) which exhibit large undercooling values. A further extension of the

droplet technique allows for direct measurement of the effect of cooling rate on the undercooling potential of the liquid. Nucleation temperatures can now be measured for cooling rates approaching 10^3 ° C/sec.

I.B Upquenching

Understanding microstructural evolution during rapid solidification of an undercooled melt requires a consideration of the effects of recalescence which results from the rapid release of the latent heat of fusion. For an undercooled liquid droplet (which can be assumed to represent an adiabatic system (12)) the maximum temperature reached during recalescence, T_R^{max}, is governed by thermodynamic considerations: the latent heat of fusion, the specific heat of the sample, and the degree of undercooling prior to the onset of crystallization. For a binary alloy, if the undercooling is large enough so that T_R^{max} is less than the solidus temperature T_S, the liquid is said to be hypercooled, and the entire droplet may solidify in a partitionless manner. Although the alloy T_0 temperature represents the thermodynamic limit to the partitionless transformation, undercooling sufficient to prevent recalescence above T_S is required to ensure that remelting of C_0 solid does not occur. Since this hypercooling condition is not frequently achieved (even for the high liquid undercooling levels attained with the DET), the solidification of undercooled melts will usually involve a stage once T_R^{max} is reached in which the growth rate of the solid is much slower. That portion of the droplet which freezes during cooling from T_R^{max} will exhibit a segregated solidification pattern as opposed to the compositionally homogeneous solid which forms in the early stages of solidification.

A schematic representation of recalescence behavior is shown in figure 1 for an alloy of composition C_0. This representation assumes solidification by slow cooling in an adiabatic system. The liquid of composition C_0 is slow cooled along path 1, and upon reaching point 2 at a temperature $T_N > T_N^{hyp}$ the undercooled liquid begins to solidify forming solid of composition C_0. As solidification is occurring heat is released sufficient to reheat the sample (along path 3)

until a maximum temperature T_R^{max} is reached, at which point cooling of the sample continues since the sample is in a surrounding environment at a temperature of T_N (due to the adiabatic assumption, the environment is not allowed to change temperature as a result of recalescence). Cooling of the sample from T_R^{max} results in the solidification of the remaining liquid fraction of the droplet according to the usual alloy solidification pathway (13). The result will be solute partitioning in that portion of the droplet solidified after T_R^{max}, with compositions of liquid and solid in equilibrium at the interface varying, respectively, along the liquidus and solidus curves from T_R^{max} to $T_S(C_o)$ (path 4). Thus, the post-solidification droplet would be expected to consist of an initial fraction solid of uniform composition and the remainder of the droplet with a segregated structure (possibly dendritic) resulting from solute partitioning along paths 3 and 4 in figure 1. As the droplet recalesces above T_S, the C_o solid which formed during the initial stage of solidification becomes metastable with respect to formation of a two-phase mixture of solid + liquid with compositions given by the equilibrium phase boundaries. Therefore, once T_R exceeds T_S, an important factor controlling T_R^{max} is the kinetic stability of the C_o solid with respect to melting. For this reason, the melting behavior of an initially homogeneous solid solution alloy during continuous heating is worthy of investigation.

I.C Dispersed Particle Catalysis

In almost all solidification processes, the crystallization of a bulk liquid volume occurs through favorable interaction between the melt and internal or residual catalysts which act as heterogeneous nuclei. The heterogeneous sites can be melt impurities or other external catalysts inherent to most casting processes. To a large extent, the initial phase selection or solidification pathway produced in a system can be altered through the operation of an intended nucleant site. Therefore, through catalysis control and associated nucleant site identification, it is possible to selectively control the phase selection process including the initial structure type, size scale, and distribution of product phases.

Effects induced from heterogeneous nucleation catalysis also exert a strong influence on the resultant grain size, phase morphology and compositional homogeneity as well. In order to modify and refine the as-cast solidification microstructure, it is common practice to intentionally inoculate a melt with particle catalysts that surpass the catalytic activity of other less potent heterogeneous nuclei in contact with the bulk liquid. By using this inoculation procedure, the added catalysts can promote the nucleation of a refined primary phase, alternative product phase morphologies, or the formation of fine equiaxed as-cast grain structures with enhanced mechanical properties.

There is a wide commercial application of cast alloy treatments that modify the initial solidification characteristics to provide a means for effective control of grain size and morphology. Examples include the addition of ferrosilicon to cast iron in order to promote the nucleation of graphite; Zr or C can be added to refine Mg alloys; P is introduced to Al-Si alloys to refine the primary Si phase size; As or Te can be added to Pb alloys; and Ti is added to Zn based systems. Other additives, such as Na in Al-Si alloys, are used to modify the growth morphology. In addition there is also a wide body of experience on the grain refinement of Al based alloys by Al-Ti and Al-Ti-B melt additions (14-26).

While the success of inoculation procedures is clearly established, the actual performance of inoculant additions in practice exhibits a fair amount of variability. For example, Al-Ti and Al-Ti-B master alloy additions that refine Al alloys are relatively complex and minor changes in the manufacturing process used to prepare them can result in significant differences in their effectiveness (22,27,28). Moreover, even though there is a broad data base of literature concerning grain refinement processing, an understanding of the actual mechanism(s) by which grain refining agents operate in a melt still remains uncertain.

The basic requirements for an effective nucleating agent can be assessed from consideration of nucleation theory (29-31). In order to promote the formation of crystals on an intended nucleant, the interface between the nucleant and the liquid should be of higher energy than that between the nucleant and the solid. This condition is maximized by providing nucleant-solid crystallographic relationships that result in low disregistry orientations between the respective

lattices. In fact, the potency of a given catalyst is believed to be increased for decreasing values of relative lattice disregistry with the crystalline phase, and results in solidification at lower levels of undercooling. However, under conditions of poor crystallographic fit, a reduction in interfacial energy may occur through chemical interaction (29), electronic interaction (32), or the formation of interfacial compounds and adsorbed reaction layers that are experimentally associated with much larger levels of undercooling (30,33,34). In addition to the basic requirement of lattice stability, to insure effective catalysis of solid, the melt should tend to wet the surface of the nucleant. Improved mutual wetting characteristics are generally associated with a decrease in substrate-liquid interfacial energy and can be affected by parameters such as substrate surface roughness (35-37), substrate porosity (38), temperature (39,40), and adsorption phenomena induced by increased chemical affinity at the interface (41) or impurity effects in the liquid and surrounding atmosphere (42-44).

As an additional prerequisite for inoculant particles used as effective grain refining agents, the onset of solidification should not be followed by a rapid crystal growth, to allow the full effect of the potential nucleants to be realized. In alloys the growth restriction may be achieved as a consequence of solute redistribution during freezing which allows for nucleants dispersed throughout the melt to become effective and favors an equiaxed grain structure (16,45,46).

Within these general requirements, a number of compounds appear to act as effective catalysts for the nucleation of Al with disregistry values below 10% and nucleation undercoolings of less than $\sim 5^{\circ}$ C (18,21,23,47). However, the exact identities of the active nucleants have not been established by direct observation, but rather the operative nucleants have been inferred from thermal and structural results obtained from standard bulk refinement tests.

The issue of specific nucleant identity is crucial when it is considered that in commercial melts, a broad spectrum of catalysts exists that may operate singly or together to yield crystallization events. The presence of uncontrolled nucleation sites can yield irreproducible catalysis results that are related to the sample environment and the population of internal particles which may be comprised of several different structural types with variable sizes, size distributions,

and surface conditions. For example, in Al castings containing refining agents which approach ideal effectiveness, the number of grains in a casting should approach the total number of inoculant particles added to a melt. However, from actual ingot grain density measurements in Al alloy castings containing inoculant additives, a grain density corresponding to only 1-2% inoculant particle effectiveness is usually observed (22). Also, it appears that small amounts of V, Cr, and Zr can act to poison catalytic particle surfaces (17,22,48).

Since the nucleation and growth characteristics of grain refinement indicate a sharp selection of particles in terms of refinement effectiveness, it is important to investigate and identify the parameters that influence the catalysis of grains and the specific physical mechanisms that govern heterogeneous nucleation processes. With bulk melts and uncontrolled sample environments, it is not clear that such a study can be accomplished in a reliable manner.

However, by using the DET to produce droplet emulsions containing incorporated particle catalysts, residual catalytic interaction between intended nucleation sites and residual sites present in bulk samples and their environments are eliminated. In addition, the ability to produce changes in droplet coating chemistries allows for the assessment of potential interactions between the particle catalysts and the applied droplet surface coatings. Analysis of the various interactions possible allows for assessment of the true catalytic potencies of intended inoculants by using differential thermal analysis (DTA) (49). Moreover, because inoculant particles are isolated into individual droplets within an emulsion sample, the DET has been used to produce powders of commercial Al master alloy grain refiners. DET processing of master alloys results in the incorporation of effective and ineffective catalyst particles within discrete droplets (50). This technique used in conjunction with analytical x-ray and microbeam studies has allowed for the subsequent identification of chemical and morphological differences between the catalytically potent and ineffective particle species (51).

II. RESEARCH ACCOMPLISHMENTS OF THE CURRENT PROGRAM

During the current program, from July 1, 1986 to June 30, 1989, research has been focused upon metastable phase formation and the controlling phase selection reactions, the evolution of solidification microstructure under the combined influence of undercooling, recalescence and external cooling and several other aspects of undercooled alloy solidification and product structure stability. The experimental approach that has been applied to carry out these studies is based on the droplet emulsion technique. With this method, samples may be produced which exhibit large undercoolings prior to solidification during slow cooling (10-30° C/min) and which may be maintained in the metastable undercooled state for extended time periods without the intervention of crystallization.

At deep undercoolings equilibrium crystallization reactions may be bypassed and metastable solid phases can be produced during freezing. With thermal analysis and x-ray diffraction measurements it has been possible to examine the undercooling conditions for metastable phase formation and to elucidate the kinetic competition during crystallization. Often, the microstructural morphology and the structure of product phases that solidify from the melt have features which are distinct to high undercooling solidification. Several examples of fine-scale eutectics, multizone structures, and ultrafine dispersoids as well as uniform, supersaturated solid solution morphologies have been identified in droplet samples.

For selected reactions it has been possible to identify the solidification path for crystallization from the undercooled liquid state. With samples containing known nucleation catalysts, thermal analysis and x-ray diffraction study have been used to identify a path for the generation of supersaturated solid solutions and metastable intermediate phases. Based on these findings it has been possible to develop a framework for describing the reaction paths followed during high undercooling solidification in terms of metastable phase diagram construction (52). In one case for the Pb-Sn system a fairly detailed and complete experimental measurement and thermodynamic modelling evaluation of the stable and metastable equilibria has been performed

(53,54). In a complementary examination, the use of droplet samples with controlled undercooling levels and known nucleation catalysts has permitted the documentation of new features governing heterogeneous nucleation (49). For example, it is often considered that the lattice disregistry in a heteroepitaxial relationship between a catalyst surface and the nucleus is the key to controlling heterogeneous nucleation undercooling, at least at low undercooling. However, at high undercooling there is now clear evidence that a chemical interaction at the catalysts surface is important in establishing catalytic potency.

Several new applications and methods involving droplet samples have also been advanced during the current research. The influence of elevated pressure on the solidification pathway in undercooled liquids has been examined in alloy droplet samples (55). The initial observations that only modest pressures are needed to alter the solidification pathway have been confirmed in alloy samples, and more importantly the altered pathway is associated with a modified microstructure. In other studies a new enhancement of undercooling that appears to be associated with rapid pressure changes has been detected. A new perspective on rate effects has also been developed in terms of both processing method and model analysis. Procedures have been established to allow for the measurement of nucleation undercooling temperatures at cooling rates approaching 10^3 ° C/sec. These results have been coupled with a nucleation kinetics model to provide a quantitative assessment of the measurement requirements for reliable analysis of nucleation rates (56).

Several advances in experimental capability have been established during the current work. An important development in the controlled upquenching of droplet samples has provided a direct measurement of metastable phase boundaries and the first reports of T_0 measurements (57). Besides dynamic experiments, new capability has been added for in-situ analysis of phase selection and the thermal stability of product structures with a new x-ray diffraction system that is equipped with a position sensitive detector for rapid data acquisition.

In addition, the droplet technique has also been modified to allow for analysis of the catalytic potency of various compounds for nucleation of a metallic phase through the incorporation of

inoculant particles into the droplets during emulsification (49). This technique is currently being used to evaluate the effectiveness of Al grain refining master alloys (50).

II.A Undercooling Behavior of Pure Metals

The droplet emulsion technique has proved to be a very effective means of attaining high levels of liquid undercooling. Present experience with the droplet method has identified a number of processing parameters that are likely to govern the optimization of undercooling in powder samples (58). These processing variables include droplet size refinement, sample purity, droplet surface coating, uniformity of coating, cooling rate and melt superheat as well as alloy composition and applied pressure. Although the influence of these processing variables has been demonstrated with droplet experiments, the results are general and are expected to apply to other processing methods where direct measurement and control of solidification is more difficult.

The effect of the various processing parameters on the undercooling response is summarized in table 1. Even when these processing conditions are satisfied to produce maximum undercooling, experience suggests that solidification is still initiated by a heterogeneous nucleation site associated with the sample surface (59). Therefore, it appears that close attention to the nature of the powder surface coating is of prime importance in achieving reproducible, large undercooling values in fine powders. The maximum undercooling limits for several pure metals measured using thermal analysis are listed in table 2. Based upon the comparison presented in table 2, current studies have demonstrated clearly that the previous maximum undercooling values actually correspond to heterogeneous nucleation conditions. Indeed, the present findings emphasize that further nucleation kinetics studies are necessary before a complete characterization of the revised undercooling limits in terms of heterogeneous or homogeneous kinetics is possible.

II.B Solidification of Al Alloy Powders

A similar influence of powder processing parameters has also been found to prevail in the treatment of Al-rich alloys as well. The solidification microstructure that develops in Al alloys has been documented to be related closely to the initial level of undercooling at the onset of solidification (60,61). Of course, with alloy solidification the available pathways for freezing from an undercooled state involve a variety of options. In this case, the microstructural and thermal history capabilities that can be applied in the controlled solidification of powder samples produced from the DET are of particular assistance in identifying the operative pathway under a given set of processing conditions. A number of the RSP pathway options can be analyzed by examining the solidification of droplet samples in several Al alloy systems, some of which offer useful potential for dispersoid formation.

Through the control of melt undercooling in Al alloy droplet emulsions, highly dispersed phase mixtures have been produced in several alloys through various phase separation reactions, fine scale eutectic growth, precipitation of phases from supersaturated solid solutions, and from the decomposition of metastable phases (62). In addition, the microstructural morphologies that develop during the solidification of the undercooled Al alloy droplets under slow cooling conditions are also comparable to the structures that evolve during the rapid quenching of atomized powders. Therefore, the information obtained from the alternative solidification pathways allowing for favorable microstructures to be developed can be used as a basis for effective RSP alloy design. A brief summary of the undercooling behavior and microstructure response for various Al alloys is given in table 3. Further details are provided in the associated publications of the current program.

II.C Heterogeneous Nucleation

The nucleation of a solid on an energetically favorable surface present within a liquid can ultimately control the solidification microstuctures and interrelated physical and mechanical properties of many materials. By examining the solidification responses generated from liquids containing a variety of identifiable catalytic sites such as primary phases, or secondary dispersed particle additions, it is possible to modify and control the solidification microstructure by altering the heterogeneous nucleation response to achieve the desired mechanical properties. In order to promote a given solidification pathway via nucleation on an intended catalyst in addition to conducting a meaningful assessment concerning the actual catalytic potency of the specified agent, it is essential that all background nucleation sites more potent than the intended agent be removed or isolated from the sample. In prior investigations, the DET was well suited for this purpose and was used to study heterogeneous nucleation responses generated through primary phase catalysis (20,63).

II.C.1 Dispersed Particle Catalysis of Sn Droplets

By incorporating compound particles into an initial Sn melt, subsequent DET processing yields a significant fraction of droplets that contain the dispersed particle addition while the remaining portion are particle free as illustrated in figure 2. Typically the dispersed particles are approximately <1 to 5μm in size and are incorporated in 1 to 20μm droplets. A variety of chemically and structurally different particle catalysts have been incorporated into Sn droplets including several oxides, sulfides, tellurides, and metalloid intermetallic compounds.

Since a variety of nucleation sites may be active within the droplets including residual impurities and the droplet coating, possible operative sites within the droplet sample must be identified. Figure 3 summarizes the principal features of the heterogeneous nucleation sites that may be active during the undercooling of a droplet/incorporated particle dispersion where site 1 is a residual isolated impurity, site 2 is the droplet coating, and site 3 is a junction site involving the

influence of the incorporated particle (site 4) and the droplet coating on the resolved catalytic activity. Based upon this description the nucleation undercooling will change in response to a change in surface coating when either site 2 or 3 is active. However, if the activity of the particle exceeds that for sites 2 and 3, the nucleation undercooling associated with the particle (site 4) will be unchanged by modifications of the droplet surface coating. Therefore, by changing the droplet surface coating and monitoring the undercooling responses of droplets emulsions containing pure droplets and particle incorporated droplets the actual catalytic potency of particle inoculants can be established.

Figure 4 illustrates this procedure in a series of DTA thermograms produced from pure Sn and Y_2O_3 particle dispersed Sn droplets. In figure 4A, pure Sn droplets nucleate at an undercooling of 176° C, while in figure 4B a Y_2O_3 emulsion produced with an identical droplet coating shows the pure Sn undercooling and an exotherm associated with catalysis by the Y_2O_3 particles at 136° C of undercooling, thus establishing the presence of both Y_2O_3 incorporated and Y_2O_3 free droplets within the emulsion. In figure 4C, a Y_2O_3 dispersed particle emulsion produced with a different droplet coating shows a shift in the pure Sn undercooling while the undercooling for droplets containing Y_2O_3 particles remains constant. Therefore junction site activity between the coating and the incorporated particles is absent and the most catalytic site present within the emulsion is the liquid/Y_2O_3 interface. However, in droplets free of Y_2O_3 particles a shift in undercooling indicates nucleation by the droplet coating. In figure 4D, an applied oxide coating shows the masking effect of background sites on the catalytic response in both Y_2O_3 incorporated and pure Sn droplets.

In droplets containing other oxide compounds, identical catalytic responses are also observed in most Sn/oxide particle incorporated droplets as shown in figure 5, while telluride compounds and some sulfide compounds also yield identical nucleation responses at different levels of undercooling for the respective interactions between the Sn/Tellurides (ΔT_n = 69° C) and Sn/Sulfides (ΔT_n = 78° C). Although it is difficult to judge the exact nature of the nucleus substrate atomic interaction, the calculated disregistry values between β-Sn and the various

compounds for a variety of low index planes do not show common values or relatively low values (i.e. < 15%), characteristic of near epitaxial conditions. However, the undercooling levels and common undercooling responses observed for each compound class (oxide, sulfide, telluride) do suggest that the role of melt-substrate interfacial reaction layer formation or adsorbtion phenomena are controlling parameters for the catalytic responses (30,33).

II.C.2 Nucleant Differentiation in Al Grain Refining Alloys

Aluminum master alloys that contain particle dispersions of Ti aluminides and Ti borides represent an important class of materials that are used as alloy additions to promote the formation of fine, equiaxed grains during the solidification of pure Al and many Al alloys castings. However, even though master alloy additions have been successfully used in commercial applications for almost four decades, mechanisms which control the physical processes of grain refinement that involve dispersed particle additions are not well understood and in practice a significant degree of refinement variability exists with their actual performance. For example, in Al castings containing refining agents which approach ideal effectiveness, the number of grains in a casting should approach the total number of inoculant particles added to the melt. However, for actual ingot grain density measurements in Al alloy castings containing inoculant additives, a grain density corresponding to only 1-2% inoculant particle effectiveness is usually observed (22).

This degree of inoculant catalytic variability and limited effectiveness is the subject of much controversy and has been attributed to factors such as fading or particulate dissolution, settling or agglomeration of inoculant particles, impurity poisoning of intended agents, or transient chemical equilibria associated with the formation of particle complexes (17,22,45). However, in bulk refined castings it is virtually impossible to identify and analyze effective inoculant particles without knowing which of the agents promote grain formation through the isolated or combined effects of the aforementioned phenomena. In fact, visual identification of the potent inoculant population in bulk refined ingots is not possible because solidification morphologies associated with the

nucleation and growth of Al on effective particle catalysts are usually consumed during matrix coarsening in slowly cooled ingots. Therefore, given a maximum 2% effectiveness in commercial inoculation efficiency, examination of typical inoculant particles within a bulk refined ingot will not yield an accurate representation of the actual nucleation parameters responsible for effective catalysis of grains by a minority of the inoculant particle population.

However, by using the DET to produce powder samples from commercial master alloys (figure 6), specific inoculant particles responsible for effective catalysis of grains can be isolated within a minor fraction of the droplet population and distinguished from the majority of less effective particles contained within most of the droplets. This is accomplished by using a series of quenching treatments during DTA cooling cycles of master alloy droplet samples. These quenching treatments preserve solidification microstructures associated with the nucleation and growth of Al off of the minor fraction of effective inoculant particles. Therefore, differences between the heterogeneous nucleation responses generated during DTA can be separated and identified with microstructural differences between droplets containing effective and ineffective inoculant particles. This procedure then allows for variables which influence the catalytic potency to be identified in specific particles. These variables may include inoculant chemistry, size, morphology or surface conditions (21,22,27,28).

Since the catalytic potency of an intended nucleation site can be characterized by the amount of undercooling prior to the onset of solidification (63), typical thermograms from a bulk sample (Figure 7A), and a droplet sample (figure 7B) of a commercial Al-6wt% Ti refining alloy produce three endothermic and exothermic events at < 660, 665, and 672° C which indicate the presence of inoculant particles of variable potency within the alloy. In the cooling traces, the exotherm at 665° C corresponds to the equilibrium peritectic reaction between Al, liquid, and Al_3Ti, as confirmed by a similar response at 665° C in laboratory specimens produced from high purity (99.99%) Al-1wt% Ti droplet emulsions (figure 7C). However, the exotherm produced in the master alloy samples at < 660° C is not present in the high purity droplet sample indicating that the thermal events occurring below 660° C are not associated with the normal solidification of Al,

but are due to the growth of a multicomponent Al eutectic, which forms during the last stages of freezing in the commercial purity master alloy. The reaction exotherm occurring at 672° C in the high purity droplet sample (figure 7C) is due to the occurrence of a metastable peritectic reaction between Al, liquid, and an intermediate Al_xTi intermetallic phase (64-66). However, in the master alloy samples EDS data shows that the presence of Si in the more catalytic particles is responsible for an increase in the equilibrium peritectic reaction temperature to 672° C. Therefore, it appears that incorporation of Si into Al_3Ti intermetallic particles provides an effective means for improving inoculant effectiveness.

Droplets containing the most potent inoculants, are identified by quenching a sample during DTA at a temperature just below the initial nucleation onset temperature (∿671° C). This treatment preserves microstructural features associated with the nucleation and growth of Al from only the most catalytic inoculants incorporated within some of the master alloy droplets. Figure 8A shows that droplets containing less effective intermetallic particles that do not contain Si are still liquid upon quenching from ∿671° C and have cellular microstructures similar to the solidification microstructures produced in droplets quenched from a temperature above both invariant reactions (700° C), as shown in figure 8B. However, in a portion of the droplets which begin to solidify prior to quenching from ∿671° C, the droplet microstructures show rounded Al dendrites radiating from the more catalytically potent inoculant particles which contain Si, as shown in figure 8C and figure 8D. The presence of interdendritic eutectic in these droplets is also evident.

In addition, a preliminary statistical analysis, produced from a total of ∿500 droplets subjected to the nucleation onset quenching treatment shows that the percentage of droplets containing particles which promote the dendritic Al morphology is comparable to the actual observed grain density measurements in bulk Al (∿1%). This result indicates that inoculant isolation produced from the DET is an effective approach for subsequent identification of potent inoculant species responsible for effective Al grain refinement. Also, particles which initiate the dendritic Al microstructure possess morphological variances which are absent from the majority of

intermetallic particles contained in most of the droplets. Intermetallic particles which contain Si possess irregularly faceted growth planes containing pockets of Al rich eutectic and have Al dendrites radiating from their surfaces; however, blocky, faceted particles which are morphologically identical to the equilibrium Al_3Ti intermetallic phase do not promote the growth of Al dendrites, as shown in figure 8D. This evidence indicates that the DET can also be used to differentiate nucleant species in Al master alloy droplets by correlating Al nucleation exotherms to inoculant morphologies and to resultant Al solidification microstructures produced from interrupted DTA quenching treatments.

II.D Metastable Phase Diagrams

One of the most attractive features of RSP is directly related to the unique microstructural morphologies that have been developed in a fairly wide variety of alloy systems. A first level of microstructural evolution is the formation of highly refined microstructural constituents such as grains, cells, and dendrites of equilibrium phases which are directly associated with the reduction in local solidification time during rapid cooling. While a refined microstructural scale is certainly a valuable product of RSP, there is a further level of modification associated with alternative metastable phases that can develop under RSP conditions. These products yield novel microstructures consisting of supersaturated solid solutions, metastable intermediate phases, or amorphous structures. Generally, it is difficult to identify the specific details of the solidification kinetics that favor novel, metastable phase microstructures. However, it is clear on the basis of thermodynamic considerations of relative stability that metastable phases form from a liquid which is undercooled below the melting temperature of a stable phase. Indeed, the formation of metastable phases is evidence that an undercooled liquid existed prior to crystal nucleation at high cooling rate even if the actual temperature was not measured.

With this perspective in mind, it is appropriate to consider some of the ways in which phase diagrams may be used to select the most suitable alloy compositions for metastable phase

formation from undercooled liquids during RSP. In conventional solidification processing, phase diagrams are used to predict product phases and to analyze solute segregation distributions based upon a partition coefficient obtained from the liquidus and solidus phase boundaries. Equilibrium phase diagrams are most useful in predicting the occurrence of stable phase products. During rapid solidification, however, the nucleation and/or growth of a thermodynamically stable phase from the liquid may be difficult depending on the details of the respective kinetics. In this case the liquidus, solidus, partition coefficient or other thermodynamic data for a metastable phase are important.

There are only a very limited number of phase diagrams available which include metastable phase boundaries indicating the temperature and concentration range of metastable phases found after quenching to low temperatures. To a large extent the metastable phase diagrams that are available are based on computer calculations to extrapolate the Gibbs energy data of the stable phases into the metastable region, e.g. for Ag-Cu and Cd-Zn (67). Most often though, there exists no experimental measurements to confirm the theoretical calculation analysis.

One strategy to obtain the metastable phase boundaries is offered by the study of liquid droplet dispersions which undercool to a large degree during slow cooling. The high levels of liquid undercooling obtained with the droplet technique permit the measurement of the thermodynamic properties of the metastable liquid (68) and product phases (69) as well as the metastable equilibrium phase boundaries at different amounts of undercooling. The knowledge of the structural and thermal properties of these phases then allows construction of a metastable phase diagram and a comparison with the thermodynamic assessment of the phase boundaries. Such a detailed phase diagram evaluation outside of the stable equilibrium condition has not been available previously.

II.D.1 Pb-Sn Alloy system

Several metastable phase boundaries in the Pb-Sn alloy system have been determined in undercooled droplets using lattice parameter and thermal analysis measurements (53). Droplet

samples were annealed above the eutectic temperature to generate a two-phase mixture of primary α-Pb solid solution and liquid. During slow cooling the liquid fraction undercools below the eutectic temperature so that a metastable equilibrium is established between the α and liquid. By monitoring high angle x-ray reflections in situ under isothermal annealing conditions, the lattice parameters of the metastable (and stable) α was determined as a function of temperature. Extrapolation of room temperature lattice parameter data into the metastable regime and correction for the temperature dependence of the lattice parameter was then used to obtain the Sn-concentration of the supersaturated α-Pb phase as a function of temperature (i.e. the metastable solidus). The metastable liquidus was obtained by a comparison of the diffracted x-ray intensity measured by the peak area at different temperatures. Because the intensity scattered by the primary phase and corrected for the temperature factor (Debye-Waller) (70) is proportional to the volume of this phase, the relative amounts of metastable solid and liquid were obtained by applying the lever rule. The x-ray intensity scattered by the α-Pb phase above the eutectic temperature where the relative amounts of solid and liquid are known was used as a calibration for the amount of primary phase. The metastable solidus and liquidus of the β-Sn solid solution were obtained in a similar fashion. It should also be noted that a special thermal cycling scheme was developed to confirm that the measurements were performed under conditions of metastable equilibrium (i.e. demonstrate reversibility of the measured temperature and concentration dependence of the lattice parameter on heating and cooling) (53).

After obtaining the metastable solidus and liquidus for the two primary phases, a metastable Pb-Sn phase diagram can be drawn and is shown in figure 9 together with the stable eutectic diagram. The metastable solidus (liquidus) for the α-phase experimentally determined in the temperature range between 183° C to 105° C (183° C to 150° C) can be extrapolated graphically as is indicated by the dashed lines. This extrapolation reaches 5° C at pure Sn and agrees very well with the lattice stability calculations indicating the melting point of fcc-Sn at 279 K (71). It is important to mention that the metastable phase diagram does not show a retrograde metastable solidus for the Pb-rich side, which might be expected for a purely geometrical extrapolation of the

stable α solidus. The experimentally obtained points for the metastable solidus and liquidus of the Sn-rich side of the diagram are included additionally in figure 9 indicating a retrograde metastable solidus for primary β-Sn + liquid mixtures.

A metastable intermediate phase, α_1, was observed to nucleate during cooling below the eutectic temperature. The α_1-phase has a bct-structure with lattice parameters a = 0.3656 nm and c = 0.4197 nm at 120° C. Thermal analysis methods were used to show that the α_1 forms by a metastable peritectic reaction involving the α solid solution and liquid at 127° C. The concentration range of the α_1-phase was determined as about 65-67 at% Sn and can be included in the phase diagram (figure 10) with the intermediate phase composition $PbSn_2$.

Based on the phase boundary determinations illustrated in figure 10, it is clear that two metastable phase equilibria have been established in the temperature range investigated. The first metastable equilibrium exists between the α and undercooled liquid which extends beyond the temperature range from 183° C to 100° C that was accessible by experiment. Below 127° C there exists a second metastable equilibrium corresponding to the nucleation of the α_1 on the supersaturated primary phase. These experiments show that it is possible to undercool the α + L mixture to different levels since a significant fraction of the droplets avoids formation of α_1 phase during cooling below 127° C.

Thermodynamic calculations (using a quasi-subregular solution model) based on the measured metastable equilibria were used to obtain information on the existence of other metastable phase boundaries (54). The general form of the expression used to calculate the excess Gibbs energy is presented in figure 11, and a plot of the parameter α illustrates the relationship between the ideal, regular, subregular and quasi-subregular solution models. The variables used in this expression are defined as follows: $\Delta^{xs}G$ is the excess Gibbs free energy, x_i is the atomic fraction of each component, w_{ij} and v_{ij} are solution parameters, R is the gas constant and T is the temperature.

In previous work, Ngai and Chang calculated the stable phase boundaries of the Pb-Sn binary system (72,73). Good agreement between the stable phase diagram and the calculated version was

observed. A comparison of the previous calculation and that of the present work shows that both models represent the stable equilibria equally well. However, differences occur between the models in calculation of the metastable $\alpha/\alpha + L$ phase equilibria (figure 12). While the calculated $\alpha/\alpha + L$ phase boundary using the model parameters of the present study are in agreement with the measured values, those using the parameters of Ngai and Chang (72,73) show a tendency towards phase separation of the α-phase (dashed line). Although the quasi-regular solution model used in the earlier work adequately described the α solution behavior up to approximately 30 at% Sn, it does not provide a quantitative description at higher Sn content. The availability of the $\alpha/\alpha + L$ phase boundary data up to 50 at% Sn allows the use of a quasi-subregular solution model and a more accurate description of the phase equilibria at lower temperatures. Indeed, it appears from experience in the Pb-Sn system that in selecting a model for the solid, the behavior of the liquid can serve as a guide.

The phase diagram involving a continuous α solid solution is shown in figure 13 and includes the corresponding T_0 curve. The shape of the α-solidus suggests phase separation occurs at lower temperature as indicated by the miscibility gap (dash-dotted line). Another metastable phase diagram is indicated in figure 14. The intermediate phase α_1 forms peritectically at 400 K and subsequently reacts with Sn-rich liquid at 297.5 K to form the fcc α-Sn phase.

In addition to the phase equilibria shown in figures 13 and 14, another metastable diagram can be calculated which involves β-Sn and β-Pb (figure 15). The (β + L) two-phase equilibria as well as the corresponding T_0 curve are indicated. A metastable eutectic reaction is found with a eutectic point at approximately 10 at% Sn and 355 K, and a metastable miscibility gap for the undercooled liquid is also obtained (dash-dotted line). In the case of the (β-Sn + L) metastable equilibrium there is no intersection with the liquid miscibility gap. Whereas, the metastable liquidus for (β-Pb + L) exhibits a metastable monotectic reaction. The solubility of Pb and Sn in the β-phase is retrograde in both cases and exhibits a maximum solubility of 2 at% Pb and 1 at% Sn respectively.

II.D.2 Sn-Bi Alloy System

The melting behavior of Sn-Bi alloy droplets during continuous heating was investigated using thermal analysis techniques and x-ray diffraction (57). Beyond the characteristic structural advantages of the emulsified powder sample for this type of experiment (noninteracting single crystals exhibiting no segregation), the use of a collection of fine powders also offers the important benefit of a statistically significant measurement due to the large population ($>10^6$ powder particles). Samples were annealed below the solidus to ensure homogeneity and then upquenched to a temperature above the liquidus temperature. A systematic evaluation of the melting process and the onset of metastable effects was attained by analyzing the dependence of the melting signal on the applied heating rate.

Variation in the heating rate brought about changes in the thermal signal corresponding to melting of the Sn-2.9 at% Bi alloy investigated. For heating rates, $\dot{T}$, of $\gtrsim 0.1°$ C/sec, a distinct break in the heating curve was observed between the solidus and liquidus temperatures indicating the presence of an additional melting event at approximately 220° C. A significant increase in the magnitude of this melting signal (relative to the remaining portion of the thermal analysis signal) was observed as the heating rate was increased. It should also be noted that at heating rates below 0.1° C/sec, the additional melting endotherm (i.e. T_I) was not observed. Similar results were also obtained for the Sn-6.0 at% Bi alloy.

Thermal analysis and x-ray diffraction results of samples heated to various temperatures between the solidus and liquidus and quenched indicate that a zone of constitutionally superheated solid is created within the droplets during rapid heating. It was also observed that this departure from equilibrium melting behavior can be achieved in droplet samples through the application of relatively modest heating rates. In fact, for heating rates of 5° C/sec or greater this constitutional superheating is sufficient to allow for the retention of significant amounts of C_o solid up to temperatures approaching its T_o temperature. Furthermore, XRD and thermal analysis results also suggest that the thermal signal detected at 220° C can be attributed to melting of retained C_o solid. The structural perfection of the high purity single crystal powder samples produced using

the droplet technique may allow for the achievement of high superheating levels by minimizing the number of active internal nucleation sites for the liquid within a majority of the droplets.

Thermodynamic solution models were developed to define the free energy functions of the Sn-Bi solid and liquid solutions (57). These models were then used to calculate the T_0 curve which represents the locus of temperatures at which the solid and liquid of a given common composition have the same Gibbs free energy. From this analysis, the Sn-rich portion of the phase diagram was obtained as is shown in figure 16. The calculated solidus and liquidus curves, which are drawn as dotted lines, agree reasonably well with the phase boundaries given by Hansen (solid lines) (74). The calculated T_0 curve, indicated on the phase diagram by the dashed line, gives T_0 temperatures of 219.0° C and 205.0° C for the Sn-2.9 at% Bi and Sn-6.0 at% Bi alloys respectively. The measured temperatures of the intermediate melting signal are also indicated for the two alloys investigated.

Two phases pocessing a common composition have the same Gibbs free energy at the T_0 temperature, and therefore, T_0 represents a limit to the partitionless transformation (4). Once the droplet sample reaches T_0 (the partitionless melting temperature) during heating, the growth of liquid present at the droplet surface or that nucleating within the C_0 solid would no longer require adjustment of the solid and liquid compositions at the interface, and the supersaturated β could then melt in a partitionless manner. It was observed that the melting event detected at T_I was identical to the type of melting signal displayed by samples of pure tin powder heated at comparable rates. In both cases the thermal signal exhibits a sharp onset followed by an isothermal arrest (neglecting a slight instrumental effect of < 0.5° C) which is characteristic of an invariant reaction. In addition, the measured temperatures of this reaction exhibit little, if any, heating rate dependence over the range investigated and agree to within 1.5° C with the T_0 temperatures calculated from thermodynamic analysis and those estimated using a dilute solution approximation (75). Based on this evidence, it is proposed that the melting event detected at T_I during continuous heating corresponds to the partitionless melting of C_0 solid retained metastably within the droplets and therefore can provide an experimental measurement of the alloy T_0

temperature.

II.E Solidification of Undercooled Droplets at Elevated Pressure

With selected alloy samples the influence of hydrostatic pressures ranging up to 400 MPa on the undercooling and nucleation behavior has been examined in the droplet dispersions. In previous work on pure Bi two main effects were observed for the influence of elevated pressure on nucleation behavior. First the application of elevated pressure to an undercooled sample promotes a phase selection transition to a metastable phase that is stabilized as an equilibrium phase at high pressure. Secondly, the modest pressures needed to alter the phase selection act to modify the operating solidification kinetics rather than to produce a dramatic change in the thermodynamic stability of phases.

As an illustration of the influence of elevated pressure to mediate the product phase selection and solidification pathway in undercooled droplets it is instructive to review some of the results of a study on Sn-Bi alloys (55). At equilibrium this is a eutectic system with components that have melting point/pressure relationships of different signs which enhances the possibility of change under applied pressure. Indeed in past work on near eutectic alloys in bulk form an intermediate phase was reported to form at pressures above 2 GPa. In the bulk sample studies a "pressure quench" method is often used in which an alloy sample is subjected to a certain pressure and temperature. It is then cooled under pressure to liquid nitrogen temperature and the pressure is lowered to one atmosphere. With this method it is assumed that no structural transformations occur during cooling or pressure relaxation.

For a hypoeutectic Sn-41.4 at% Bi alloy, two types of droplet undercooling behavior were observed as noted in figure 17. In trace 1 for a maximum undercooling sample a metastable melting endotherm at T_m' was detected in addition to the stable eutectic and liquidus endotherms. For a sample with less than maximum undercooling (trace 2) only the equilibrium melting reaction was observed. When the thermal cycling was carried out at elevated pressures for the sample in

trace 2, several important changes were detected as shown in figure 18. For pressure increases up to about 150 MPa the nucleation temperature decreased and only equilibrium melting signals were detected. Above about 150 MPa, a transition in phase selection developed with the appearance of a metastable melting endotherm and an increase in nucleation temperature with increasing pressure. It is also worthwhile to note that the relative magnitude of the metastable melting endotherm increased relative to the equilibrium melting endotherms with increasing pressure. This indicates that with increasing pressure the modification of the solidification kinetics allowed for an increased fraction of the droplet population to nucleate the metastable phase. These results are summarized in figure 19 in terms of an experimentally determined P-T diagram for the Sn-41.4 at% Bi alloy. At low pressures when equilibrium phases form the nucleation temperature follows the trend of the liquidus with pressure. Above the phase selection transition at 150 MPa, the nucleation temperature follows the trend of the metastable endotherm. In fact the melting temperature trends with pressure indicate that the metastable phase would become stable above about 1 GPa. These results confirm the previous work on pure Bi and suggest that the operation of pressure modified solidification kinetics may be general.

The pressure induced modification of solidification kinetics also yielded an interesting microstructural modification. Based on x-ray diffraction the metastable phase droplets were single phase structures, but during holding at room temperature a decomposition into a fine scale mixture of β-Sn and Bi occurred. With continued room temperature holding the fine scale mixture also underwent a discontinuous coarsening. As a result the pressure quench method used in past studies may not have retained the high pressure phase completely and may be the reason for the conflicting reports of structural identity for this phase. In fact, the Sn-Bi system appears to be a good candidate for in-situ x-ray diffraction study.

Some progress has also been made in the study of rate effects involving pressure on the undercooling and nucleation behavior. There are a few reports in the literature that suggest that rapid pressure changes may influence undercooling. For example, Sekhar et. al (76) pressurized a Pb-Sn alloy up to about 3.5 GPa in 0.2 sec and reported a microstructure which is similar to that

observed in the same alloy after melt spinning. The fundamental understanding of the relationships between the rate of pressure change and undercooling is not apparent at present, but some of the reported effects may be related to an enhanced heat transfer between the sample and its container that is promoted by the application of high pressure.

The influence of rapid pressure change rates can be evaluated in the present high pressure DTA apparatus without complications due to altered heat transfer. The experiment and strategy of the approach can be understood by reference to figure 20. which shows the melting point and nucleation temperature trend with pressure for a metal such as Bi. A liquid droplet sample is pressurized and undercooled to point B which is above the nucleation onset. The sample is then rapidly depressurized at a rate of about 1 GPa/sec. Actually, since the present system for achieving high pressure is an oil based hydraulic design, the rapid depressurization results in a transient cooling so that even when the initial temperature is above the nucleation onset the actual sample temperature during the pressure drop will fall below the T_N curve.

An actual thermogram trace from a pressure drop experiment is presented in figure 21. The top recording (trace 1) shows the equilibration of the sample (dotted curve) and the reference (solid curve) at 186° C and 350 MPa. In trace 2 the pressure drop to 1 atm. results in a temperature drop to 174.5° C which recovers back to 186° C due to external heating by the DTA furnace after about 20 seconds. The sample and reference cells recover at slightly different rates due to differences in heat capacity. The nucleation onset for this sample is 184° C at 1 atm so that the sample temperature was below the onset for more than 10 seconds. After the temperature recovered to 186° C, a cooling cycle revealed a full nucleation exotherm indicating that almost all of the droplet sample survived the pressure drop without crystallization. This was confirmed further by another run in which the sample was subjected to the same pressure drop from 186° C and 350 MPa, but was heated through the melting point after the temperature had recovered to 186° C. In this case no melting signal was detected so that no crystallization occurred during depressurization.

Although these results are regarded as preliminary and are shown here to illustrate the

experimental method and research potential, they do suggest that with a rapid pressure change (i.e. depressurization) an increment of extra undercooling of about 10° C below the nucleation onset can be attained for several seconds with negligible amount of crystallization. It can also be noted that the results have been reproduced numerous times with Bi as well as with other metals such as Sn. The explanation for the effect in terms of nucleation theory is not clear at this time, but the behavior is intriguing and worthy of further study.

II.F Droplet Nucleation Kinetics

A more quantitative determination of the effect of melt cooling rate and droplet size on the undercooling level can be achieved through an investigation of the crystallization kinetics. It should be noted that the results of numerical nucleation rate calculations are highly dependent upon the values assigned to the kinetic parameters, and accurate, independent experimental determination of several of these parameters (such as the nucleation site potency and density and the interfacial energies) is not possible at the present time. However, a consideration of several cases involving limiting conditions of crystal nucleation can be used to develop a number of useful guiding relationships.

II.F.1 Isothermal Conditions

The nucleation of a solid phase from the liquid is a fluctuation process involving small clusters of atoms. These clusters vary in size and each can be considered to be a potential nucleus for continued growth of the solid. Clusters of the critical size necessary to nucleate the new phase are produced by the addition and dissolution of individual atoms. At steady state the distribution of cluster sizes is stationary, and the nucleation rate is constant. The mechanism through which nucleation of the crystalline phase occurs is usually classified into two general types. Homogeneous nucleation refers to the case in which nucleation occurs throughout the volume of liquid without an association with catalytic sites. For the majority of processing conditions,

nucleation is initiated at some catalytic site and is referred to as heterogeneous nucleation. These sites may be distributed within the volume of liquid or on the droplet surface. Based upon classical theory (77) a general expression for the steady state nucleation rate, J_i, can be represented as

$$J_i = \Omega_i \exp[-\Delta G^* f(\theta)/kT] \qquad (1)$$

where J_i relates to either heterogeneous surface nucleation, J_a; homogeneous nucleation, J_v; or heterogeneous nucleation on catalytic sites distributed within the volume, J_s. Appropriate values for the prefactor, Ω_i, activation energy barrier, ΔG^*, and contact angle function, $f(\theta)$, are used in equation (1) and kT has the usual meaning. The terms for Ω_i involve a product of the nucleation site density on a sample surface or volume basis, the number of atoms on a nucleus surface and a liquid jump frequency. For many cases $\Omega_v = 10^{30}\eta^{-1}$ $cm^{-3}s^{-1}$ and $\Omega_a = \phi 10^{22}\eta^{-1}$ $cm^{-2}s^{-1}$ with the liquid shear viscosity in poise, η, given by

$$\eta = 10^{-3.3} \exp[3.34T_l/(T-T_g)] \qquad (2)$$

where T_l is the liquidus temperature and T_g is the glass transition temperature (78). The term ϕ in the expression for Ω_a is defined as the fraction of surface sites which are active. For J_v and J_a, ΔG^* is given by $\Delta G^* = b\sigma^3/\Delta G_v^2$ where σ is the liquid-solid interfacial energy, ΔG_v is the driving free energy for nucleation of a unit volume of product phase and $b = 16\pi/3$ for spherical nuclei with $f(\theta) = 0.25[2-3\cos\theta+\cos^3\theta]$. For heterogeneous volume nucleation the value of Ω_s depends on the specific catalyst concentration and size as well as the form of ΔG^* which is related to the details of the catalyst-nucleus interaction (79).

The nucleation rate is a relatively steep function of temperature with a magnitude determined principally by the exponential term involving ΔG^* at the nucleation temperature , T_n and to a lesser degree by the prefactor term. In evaluating the temperature dependence of J_i, usually a constant value is taken for Ω_v, but for Ω_a and Ω_s it is necessary to consider that the catalytic site density may vary for different conditions. Similarly, since little information is available to estimate the catalytic potency of a particular site, a range of $f(\theta)$ values is normally used in calculations. However, the most important parameters in determining J_i and hence the maximum undercooling level are ΔG_v and σ which have received continued experimental and

theoretical study (68,80,81).

In general, the critical condition to observe nucleation experimentally during isothermal holding over a time t (usually one nucleus per sample) is $J_v vt = 1$, $J_a at = 1$ or $J_s st = 1$ depending on the nucleation kinetics controlling solidification. Therefore, using equation (1) the time for experimentally observable nucleation under isothermal conditions, t_i, (assuming heterogeneous surface kinetics) can be written as

$$\ln(t_i) = -\ln(a\Omega_a) + \Delta G^* f(\theta)/kT \qquad (3)$$

or

$$\ln(t_i) = -\ln(a\Omega_a) + 16\pi\sigma^3 f(\theta)/3k\Delta H^2 T_m T_r (1-T_r)^2 \qquad (4)$$

where a is the droplet surface area, ΔH is the heat of fusion, T_m is the melting temperature and T_r is the "reduced undercooling" defined as $T_r = T_n/T_m$ where T_n is the nucleation temperature. It should also be noted that a lower bound for the onset of nucleation of a crystalline phase has been estimated to be $T_r = 1/3$ (9).

The effect of droplet size on the nature of the nucleation process can be estimated through an evaluation of equation (1). A consideration of the conditions necessary for ($J_v vt$) and ($J_a at$) to be of comparable magnitude (for a given sample size) can be used to determine the transition point between heterogeneous surface and homogeneous volume dependent nucleation (60). For a monodisperse droplet size one can write the ratio J_a/J_v as

$$J_a/J_v = [\Omega_a/\Omega_v] \exp[\Delta G^*(1-f(\theta))/kT] = v/a \qquad (5)$$

where v and a correspond to the droplet volume and area respectively. Assuming $\Omega_v = 10^{35}$ $cm^{-3}s^{-1}$ and $\Omega_a = 10^{27}$ $cm^{-2}s^{-1}$ and using the limiting value for the onset of sensible nucleation ($\Delta G^* = 60kT$), the ratio J_a/J_v can be written as a function of $f(\theta)$ (figure 22). Figure 23 illustrates that for a 20 μm droplet ($v/a = 3.3 \times 10^{-4}$ cm), at a critical contact angle, θ_t, of 118° there is an equal probability for the heterogeneous surface and homogeneous volume nucleation processes. Homogeneous nucleation would be favored over heterogeneous nucleation for catalysts exhibiting

a potency which can be described by contact angles in excess of 118°. It should be noted that this analysis also assumes a constant active surface site fraction of $\phi = 1$.

Another feature to consider when examining the conditions necessary to observe a transition in the nucleation kinetics is the influence of a possible range of catalytic site densities represented by variation of Ω_a in equation (4) as well as changing catalytic potencies reflected by variation of $f(\theta)$. The effect of these variables on the appearance of a kinetic transition is illustrated by the series of isothermal time-temperature-transformation curves shown in figure 23. In both cases the dashed curve represents homogeneous nucleation. For a relatively low catalyst site density ($\Omega_a/\Omega_v \simeq 10^{-20}$), a kinetic transition from heterogeneous surface to homogeneous volume nucleation is possible depending on the potency of the active catalyst (figure 23a). On the other hand a relatively high site density ($\Omega_a/\Omega_v \simeq 10^{-10}$) would, in general, preclude the observation homogeneous nucleation as is illustrated in figure 23b. The conditions examined in figure 23 demonstrate that a given undercooled volume does not have to be free of all nucleants in order to achieve a transition to homogeneous kinetics. It is only necessary that the degree of dispersal is sufficient to mitigate the influence of the most potent nucleants.

When a liquid sample is solidified in a highly undercooled condition, the nucleation process becomes the rate determining step for solidification. Therefore, the nucleation rate is equivalent to the solidification rate. In a fine droplet dispersion, the nucleation event in each droplet is an independent occurrence. On this basis a first order reaction law can be applied to describe the rate of solidification in a distribution of droplets (77) as

$$dN(v_i,t)/dt = -k_i N(v_i,t) \qquad (6)$$

or

$$N(v_i,t) = N(v_i,0) \exp(-k_i t) \qquad (7)$$

where $N(v_i,t)$ is the number of liquid droplets belonging to the ith size group at time t with volume v_i and k_i is the operative nucleation frequency. For homogeneous nucleation, $k_i = J_v v_i$, and for the more commonly observed surface area dependent heterogeneous nucleation, $k_i = J_a a_i$ where a_i is the surface area of a droplet with volume v_i.

The time dependence of the liquid droplet distribution or the freezing rate is illustrated schematically in figure 24 for isothermal conditions. Initially at $\tau = 0$ the liquid droplet size distribution is log-normal. As time passes larger droplets freeze before smaller sizes at a rate given by equation (6). As a result the initial distribution characteristics of liquid droplets changes as shown in figure 24. The rate of this size distribution change will be different for volume dependent and surface area dependent kinetics and can be measured experimentally to determine the operative nucleation mechanism.

Most often a droplet sample contains a distribution of nucleants either internal or on the surface which can become active during cooling. The droplet fraction which is free of such nucleants can be evaluated from the Poisson distribution function. Under these conditions the number of liquid droplets of volume v_i that remain in a distribution after cooling from T_m to T_n can be obtained as

$$N(v_i,0) = N_T P(v_i) \exp(-m_i a_i) \qquad (8)$$

where N_T is the total number of droplets, $P(v_i)$ is the log-normal distribution function (82) and m_i is the number of surface catalysts per unit area. The isothermal solidification of a droplet dispersion is then described by the total number of unfrozen droplets at time t, $N_T(t)$, as the summation of nucleation events over all size classes

$$N_T(t) = N_T \Sigma_i P(v_i) \exp(-m_i a_i) \exp(-J_a a_i t) \qquad (9)$$

In practice, $N_T(t)$ can be monitored by calorimetric (83), dilatometric (77) or direct observation measurements (84).

II.F.2 Continuous Cooling

During continuous cooling the critical nucleation condition (e.g. $J_a at = 1$) requires some modification to account for the total number of nuclei, N, formed while cooling from T_m to T_n (85). Assuming a constant cooling rate, $\dot{T}$, N can be written as

$$N = -(1/\dot{T}) \int_{T_m}^{T_n} J_i(T)\, dT \qquad (10)$$

where $J_i(T)$ is the nucleation rate at temperature T. The integration involved in equation (10) is the area under the curve in figure 25. Although this area can be evaluated numerically, it can be approximated by the shaded region as

$$-\int_{T_m}^{T_n} J_i(T)\, dT \simeq (T'-T_n)\, J_i(T_n) \qquad (11)$$

where T' is the intersection between the tangent to $J_i(T)$ at T_n and the T axis. Assuming that σ and Ω_i are independent of temperature over the narrow range of interest, differentiation of equation (11) with respect to temperature gives

$$T' = T_n - \frac{\Delta G_v^3 T_n^2}{A(2T_n\, d\Delta G_v/dT + \Delta G_v)} \qquad (12)$$

where $A = 16\pi\sigma^3 f(\theta)/3k$. For the case of heterogeneous surface nucleation, the critical condition to observe nucleation during continuous cooling can now be written as

$$J_a(T_n)\text{at} = \frac{-A\Delta T(2T_n\, d\Delta G_v/dT + \Delta G_v)}{\Delta G_v^3 T_n^2} = K(T_n) \qquad (13)$$

where $t = \Delta T/\dot{T}$. Typically, $K(T_n)$ is on the order of 10^2 for $0.6 \le T_r \le 0.7$ (60). From this analysis, the time required to observe heterogeneous nucleation during cooling, t_c, is given by

$$\ln(t_c) = -\ln[a\Omega_a/K(T_n)] + 16\pi\sigma^3 f(\theta)/3k\Delta H^2 T_m T_r (1-T_r)^2. \qquad (14)$$

The comparison of equations (4) and (14) indicates that the ratio $t_c/t_i \simeq 100$. In other words, the transformation curve for continuous cooling will be shifted to longer times with respect to the corresponding isothermal curve. A central assumption of this analysis is the maintenance of steady state conditions over a range of nucleation temperatures where the approximation of equation (11)

is reasonable. It should be noted that for large ΔT and high $\dot{T}$ transient conditions are likely to become important in determining the rate of kinetic responses.

For a given Ω_a/Ω_v ratio, variation of the $f(\theta)$ term in equation (14) can be used to generate a series of transformation curves identical to those calculated from equation (4) for the isothermal case (figure 23). These curves may be used to explain the difference in undercooling behavior displayed by tin and indium droplet samples (58). The sequence of crystallization exotherms exhibited by the tin sample suggests that a spectrum of nucleants of varying catalytic potency is present within the liquid. It is clear that the active nucleants are not all equally effective in catalyzing solidification and are not distributed in equal abundance. The occurrence of crystallization exotherms at similar temperatures in different droplet dispersions would suggest that in each case a common nucleation site initiated solidification. The development of exotherms at distinct undercooling levels implies that each of these sites may be characterized by discrete values of $f(\theta)$. Melts containing catalytic sites with potencies described by a continuum of $f(\theta)$ values would be expected to exhibit an undercooling response like that of indium.

A series of schematic continuous cooling transformation curves is given in figure 26 to illustrate the application of transformation diagrams for analyzing crystallization kinetics (60). Curve A corresponds to formation of a metastable phase, and the curves B, C and D refer to nucleation of the equilibrium phase. Transformation curve C represents the most catalytic sites. As the value of $f(\theta)$ increases, i.e. the potency decreases, the curve breadth tends to decrease, and the nose shifts to shorter times. The dashed lines in figure 26 represent typical continuous cooling paths. The undercooling limit for a cooling rate of $\dot{T}_1$ would be given by the intersection of the cooling path with transformation curve C. However, if the cooling rate is increased to $\dot{T}_2$, the effect of catalyst C can be negated. Therefore, the undercooling level achieved can be increased dramatically by increasing the cooling rate. The breath of the transformation curve associated with metastable phase formation, A, is larger than that for the equilibrium phase, B. If nucleants of higher catalytic potency are not present, i.e. curves C and D are absent, nucleation of the metastable phase will dominate regardless of the applied cooling rate. It is also possible for the

nucleation of the equilibrium phase to be favored with increasing cooling rate. This can occur if the nucleation site density for the equilibrium phase, curve D, is greater than that of the metastable phase, A. Under these conditions, an increase in the cooling rate would result in a reduced amount of metastable phase formation.

The approach to continuous cooling transformation kinetics outlined above has recently been applied to analyze metastable x-phase formation in a Pb-56 at% Bi alloy (86). In this alloy extensive undercooling occurs (T_r = 0.7) yielding nucleation of a metastable single phase product with a well defined crystallization onset, and measurements using DSC indicate that T_n decreases from 265 K to 255 K over a cooling rate range of 10 to 320 K/min. The continuous cooling nucleation results can be fitted to equation (14) in terms of a single nucleation frequency with a slope of 1.74×10^{7} $KJ^2 cm^{-6}$ and a value for $\Omega_a a/K(T_n)$ of 3.3×10^{22} s^{-1}. Instead of the usual approximation for $\Delta G_v = \Delta H(1-T_r)$, the ΔG_v values used were derived from direct calorimetric measurements of the latent heat of the metastable x-phase, the temperature dependence of ΔC_p and reported molar volumes. The prefactor term, Ω_a is in reasonable agreement with the classical theory result if only a portion of the surface area represents an active catalytic site for metastable phase nucleation (i.e. $\phi \simeq 0.01$).

If Ω_a, σ and $f(\theta)$ are treated as constant, evaluation of equation (14) can be used to develop the transformation diagram based on $J_a$at = 1 that is shown in figure 27. Although the calculation should be treated as approximate since estimates were used for several of the parameters, the results do illustrate some interesting features regarding the transformation kinetics. For example, if the linear approximation for ΔG_v had been applied instead of the measured values, the nose of the transformation diagram would be located at T_r = 1/3 or 128 K rather than 187 K. Also, the cooling rates required to reach the nose of the curve differ by a factor of 10^3 for the different ΔG_v values. This observation reveals the importance of using measured values for the nucleation parameters even if they represent a limited temperature range. It is also of interest to compare the droplet kinetics behavior with rapid quenching results. In this regard the calculated transformation diagram is consistent with the observation that suppression of the metastable phase by splat

quenching is difficult (87). According to figure 28 a critical cooling rate in excess of 5 x 10^7 K/s is required to bypass x-phase nucleation. Further, other droplet results indicate that another nucleation site for the metastable phase is active at a greater undercooling than that shown in figure 27. As a result, at high cooling rates a transition from one type of nucleation site to another for formation of the same phase is possible.

III. PUBLICATIONS OF THE CURRENT PROGRAM

During a research program, substantial time intervals often elapse between the completion of a research study, submission of a manuscript, and the final appearance of a paper in print. As a result, the following list gives publications in preparation as well as those in print or in press.

1. "Rapid Solidification of Highly Undercooled Aluminum Powders", J.H. Perepezko, S.L. LeBeau, B.A. Mueller and G.J. Hildeman, ASTM STP 890 ASTM, 118, (1986).
2. "Role of Nucleation In Rapid Solidification", J.H. Perepezko, In Science and Technology of the Undercooled Melt, Eds. P.R. Sahm, H. Jones and C.M. Adam, p. 29, Nijhoff, Holland (1986).
3. "Kinetics of Resolidification", J.H. Perepezko and W.J. Boettinger, In Surface Alloying by Ion, Electron and Laser Beams, Eds. L.E. Rehn, S.T. Picraux and H. Widersich, p. 51, ASM, Metals Park, OH (1986).
4. "Undercooling and Rapid Solidification of Al Powders", B.A. Mueller and J.H. Perepezko, In Aluminum Alloys: Their Physical and Mechanical Properties, Eds. E.A. Startke, Jr. and T.H. Sanders, Jr., p. 201, EMAS, West Midlands, UK (1986).
5. "The Effect of Pressure on Phase Selection During Nucleation in Undercooled Bismuth", W. Yoon, J.S. Paik, D. LaCourt and J.H. Perepezko, J. Appl. Phys., **60**, 3489 (1986).
6. "The Undercooling of Aluminum", B.A. Mueller and J.H. Perepezko, Met. Trans., **18A**, 1143 (1987).

7. "Phase Selection During Pulsed Laser Annealing of Fe-V Alloys", J.H. Perepezko, D.M. Follstaedt and P.S. Peercy, Proc. Mat. Res. Soc. Symp., **74**, 161 (1987).

8. "The Solidification of Al-Mn Powders", B.A. Mueller, R.J. Schaefer and J.H. Perepezko, J. Mat. Res., **2**, 809 (1987).

9. "Rapid Solidification of Highly Undercooled Liquids", J.H. Perepezko, J.A. Graves and B.A. Mueller, In Processing of Structural Metals by Rapid Solidification, Eds. F.H. Froes and S.J. Savage, p. 13, ASM, Metals Park, OH (1987).

10. "RSP Pathways for Alloy Design", J.H. Perepezko, B.A. Mueller and J.A. Graves, In Rapid Solidification Processing: Principles and Technologies IV, Eds. R. Mehrabian and P.A. Parrish, p. 99, Claitors Pub., Baton Rouge, LA (1988).

11. "Microstructure Development in Undercooled Al-Al_2Cu Alloys", B.A. Mueller and J.H. Perepezko, Mat. Sci. Eng., **98**, 153 (1988).

12. "Metastable Phase Equilibria and Solid State Amorphization", J.H. Perepezko, Y.A. Chang, H.J. Fecht and M.X. Zhang, J. Less Common Metals, **140**, 287 (1988).

13. "Nucleation Catalysis by Dispersed Particles", M.K. Hoffmeyer and J.H. Perepezko, Scripta Met., **22**, 1143 (1988).

14. "Experimental Evaluation of Metastable Equilibria in the Pb-Sn System", H.J. Fecht, M.X. Zhang, Y.A. Chang and J.H. Perepezko, Met. Trans., **20A**, 785 (1989).

15. "Computer Modeling of Metastable Phase Equilibria in the Pb-Sn System", H.J. Fecht, M.X. Zhang, Y.A. Chang and J.H. Perepezko, Met. Trans., **20A**, 795 (1989).

16. "Undercooling of Aluminum Alloys", J.H. Perepezko and D.U. Furrer, In Dispersion Strengthened Aluminum Alloys, Eds. Y.W. Kim and W.M. Griffith, p. 77, TMS, Warrendale, PA (1988).

17. "The Effect of Pressure on Metastable Phase Formation in the Undercooled Bi-Sn System", W. Yoon and J.H. Perepezko, J. Mat. Sci., **23**, 4300 (1988).

18. "Evaluation of Inoculant Efficiency in Al Grain Refining Alloys", M.K. Hoffmeyer and J.H. Perepezko, Scripta Met., **23**, 315 (1989).

19. "Nucleant Differentiation in Al Grain Refining Alloys", M.K. Hoffmeyer and J.H. Perepezko, In Light Metals 1989, Ed. P.G. Campbell, p. 913, TMS, Warrendale, PA (1989).

20. "Processing of Undercooled Melts", J.H. Perepezko and W.P. Allen, In Proc. Third Int. Coll. on Drops and Bubbles, Ed. T.Wang, AIP, (in press).

21. "Melting Behavior of Sn-Bi Alloy Droplets During Continuous Heating", W.P. Allen and J.H. Perepezko, Scripta Met., **23**, 643 (1989).

IV. PRESENTATIONS

1. "Solidification of Highly Undercooled Liquids", TMS-AIME Annual Meeting (1986).
2. "Rapid Solidification of Undercooled Liquids", ASM Fall Meeting (1986).
3. "RSP Pathways for Alloy Design", Rapid Solidification Processing: Principles and Technologies IV, Santa Barbara, CA (1986).
4. "Experimental Evaluation of Metastable Phase Equilibria", TMS-AIME Annual Meeting (1987).
5. "Undercooling of Al Alloys", TMS-AIME Annual Meeting (1988).
6. "Metastable Phase Equilibria in Al Alloys", TMS-AIME Fall Meeting (1988).
7. "Nucleation Kinetics-Current Status", Workshop on Solidification Microstructures, Zermatt Switzerland, July 1988.
8. "Solidification of Solder Alloys", Solderability Workshop, North American Rockwell-Science Center, August 1988.
9. "Microstructure Evolution During Rapid Solidification", DARPA Workshop on Mathematical Modeling of Materials Processing, Greenbriar, W. Va, 1988.
10. "Metastable Phases in Materials Processing", Containerless Processing of Metals-Undercooling and Solidification, Aachen, W. Germany, 1988.

V. PARTICIPATING SCIENTIFIC PERSONNEL

1. Professor J.H. Perepezko, Principal Investigator
2. Dr. H. Fecht, Postdoctoral Fellow
3. W.P. Allen, Graduate Student, MS in Aug. 1986, currently working on PhD
4. M.K. Hoffmeyer, Graduate Student, MS in Aug. 1985, currently working on PhD
5. D.U. Furrer, MS in June 1988
6. W.Y. Yoon, PhD in May 1987
7. P. Waldschmidt, currently working on MS
8. B.A. Mueller, PhD in Dec. 1986

VI. REFERENCES

1. B. Chalmers, Principles of Solidification, Wiley, NY (1964).
2. M. Cohen, B.H. Kear and R. Mehrabian, In Rapid Solidification Processing: Principles and Technologies II, R. Mehrabian, B.H. Kear and M. Cohen, Eds., Claitors Pub., Baton Rouge, LA, 1 (1980).
3. J.H. Perepezko, ref. 2, p. 56.
4. J.W. Cahn, ref. 2, p. 24.
5. W.J. Boettinger, In Rapidly Solidified Amorphous and Crystalline Alloys, B.H. Kear, B.C. Giessen and M. Cohen, Eds., Elsevier Sci. Pub., Amsterdam, 15 (1982).
6. J.J. Richmond, J.H. Perepezko, S.E. LeBeau and K.P. Cooper, In Rapid Solidification Processing: Principles and Technologies III, R. Mehrabian, Ed., NBS, Washington, DC, 90 (1983).
7. K.P. Cooper, I.E. Anderson and J.H. Perepezko, "Proc. 4th Int. Conf. on Rapidly Quenched Metals", Eds. T Masumoto and K. Suzuki, p. 107, Japan Inst. Metals, Sendai (1982).
8. T.Z. Kattamis and M.C. Flemings, Trans. AIME, **236**, 1523 (1966).

9. J.H. Perepezko and J.S. Paik, ref. 5, p. 49.

10. J.H. Perepezko, Mat. Sci. Eng., **65**, 125 (1984).

11. J.H. Perepezko, S.E. LeBeau, B.A. Mueller and G.J. Hildeman, In Rapidly Solidified Powder Al Alloys, E.A. Starke and M.E. Fine, Eds., ASTM-STP 890, Philadelphia, PA, 118 (1985).

12. C.G. Levi and R. Mehrabian, Metall. Trans. A, **13A**, 221 (1982).

13. H.D. Brody and M.C. Flemings, Trans. AIME, **236**, 615 (1966).

14. A. Cibula, J. Inst. Met., **76**, 321 (1950), **80**, 11 (1951-1952).

15. F.A. Crossley and L.F. Mondolfo, Trans. AIME, **141**, 1143 (1951).

16. I.G. Davies, J.M. Dennis, and A. Hellawell, Met. Trans., **1**, 275 (1970).

17. G. P. Jones and J. Pearson, Met. Trans., **7B**, 223 (1976).

18. J.A. Marcantonio and L.F. Mondolfo, J. Inst. Met., **98**, 23 (1970).

19. I. Maxwell and A. Hellawell, Acta Met., **23**, 895 (1975).

20. J.H. Perepezko, and S.E. LeBeau, in Aluminum Transformation Technology and Its Applications, C.A. Pampillow, H. Biloni, and L.F. Mondolfo, Eds., ASM, Metals Park, OH, 309 (1982).

21. L. Arnberg, L. Backerud, and H. Klang, Met. Tech., **9**, 1 (1982), **9**, 7 (1982)

22. M.M. Guzowski, G.K. Sigworth, and D.A. Sentner, Met. Trans., **18A**, 603 (1987).

23. J. Cisse, G.F. Bolling, and H.W. Kerr, J. Cryst. Growth, **B-14**, 777 (1972).

24. L. F. Mondolfo, in Grain Refinement in Castings and Welds, G.J. Abbaschian and S.A. David, Eds., TMS, 3 (1983).

25. D.A. Granger, "Practical Aspects of Grain Refining Aluminum Alloy Melts", Laboratory Report 11-1985-01, Aluminum Company of America, (1985).

26. J.L. Kirby, in Aluminum Alloys-Physical and Mechanical Properties, E.A. Starke and T.H. Sanders, Eds., **1**, EMAS, West Midlands, U.K., 61 (1986).

27. A.J. Cornish, Met. Sci., **9**, 477 (1975).

28. T.W. Clyne and M.H. Robert, Met. Tech., 177 (1980).

29. D. Turnbull and B. Vonnegut, Ind. Eng. Chem.,**44**, 1292 (1952).

30. P.B. Crosley, A.W. Douglas, and L.F. Mondolfo, The Solidification of Metals, Iron and Steel Inst., 10 (1968).

31. A. Hellawell, Solidification and Casting of Metals, The Metals Society, 161 (1979).

32. W.A. Tiller and T. Takahashi, Acta Met., **17**, 483 (1969).

33. C.C. Wang and C.S. Smith, Trans. AIME, **188**, 136 (1950).

34. M.K. Hoffmeyer, M.S. Thesis, University of Wisconsin-Madison (1985).

35. B.E. Sundquist and L.F. Mondolfo, Trans. AIME, **221**, 607 (1961).

36. K.A. Jackson and C.E. Miller, J. Cryst. Growth, **40**, 169 (1977).

37. D.P. Woodruff, The Solid-Liquid Interface, Cambridge Univ. Press, London, 25 (1973).

38. G.V. Samsonov, A.D. Pansasyuk, and G.K. Kozina, Sov. Powder Met. and Met. Ceram., **11**, 874 (1968).

39. S.K. Rhee, J. Amer. Ceram. Soc., **53**, [7], 386 (1970).

40. G.A. Yasinskaya, Poroshkovaya Met., **7**, [43], 53 (1966).

41. M. Humenik Jr. and W.D. Kingery, J. Amer. Ceram. Soc., **37**, [1], 18 (1954).

42. Y.U. Naidich, and G.A. Koleschenko, Poroshkovaya Met., **2**, 76 (1968).

43. Y.U. Naidich and Y.N. Chuvashov, J. Mat. Sci. **18**, 2071 (1983).

44. V.K. Nagesh, A.P. Tomsia, and J.A. Pask, J. Mat. Sci., **18**, 2173 (1983).

45. J.A. Marcantonio and L.F. Mondolfo, Met. Trans., **2**, 465 (1971).

46. A. Cibula, Foundry Trade Jnl., **93**, 695 (1952).

47. K.F. Kobayashi, S. Hashimoto, and P. Shingu, Z. Metallkde., **74**, 751 (1983).

48. G.P. Jones, in "New Ideas on the Mechanism of Heterogeneous Nucleation in Liquid Aluminum", NPL Report DMA(A) 19, Oct. (1980).

49. M.K. Hoffmeyer and J.H. Perepezko, Scripta Met., **22**, 1143 (1988).

50. M.K. Hoffmeyer and J.H. Perepezko, Scripta Met., **23**, 315 (1989).

51. M.K. Hoffmeyer and J.H. Perepezko, In Light Metals 1989, P.G. Campbell, Ed., TMS, 913 (1988).

52. J.H. Perepezko and W.J. Boettinger, Proc. Mat. Res. Soc. Symp., **19**, 223 (1983).

53. H.J. Fecht and J.H. Perepezko, Met. Trans. (in press).

54. H.J. Fecht, M.X. Zhang, Y.A. Chang and J.H. Perepezko, Met. Trans., (in press).

55. W. Yoon and J.H. Perepezko, J. Mat. Sci., **23**, 4300 (1988).

56. J.H. Perepezko, B.A. Mueller, and K.O. Ohsaka, In Undercooled Alloy Phases, E.W. Collings and C.C. Koch, Eds.,TMS-AIME, Warrendale, PA, 289 (1987).

57. W.P. Allen and J.H. Perepezko, Scripta Met., **23** 643 (1989).

58. J.H. Perepezko and W.P. Allen, In "Proc. of the Third Int. Coll. on Drops and Bubbles", T. Wang, Ed., Amer. Inst. of Phys., (1989).

59. J.H. Perepezko, J.A. Graves, and B.A. Mueller, In Processing of Structural Metals by Rapid Solidification, F.H. Froes and S.J. Savage, Eds., ASM, Metals Park, OH, 13 (1987).

60. W.J. Boettinger and J.H. Perepezko, In Rapidly Solidified Crystalline Alloys, S.K. Das, B.H. Kear, and C.M. Adams, Eds., TMS-AIME, Warrendale, PA, 21 (1985).

61. J.H. Perepezko and W.J. Boettinger, In Surface Alloying by Ion, Electron, and Laser Beams, L.E. Rehn, S.T. Picraux, and H. Wiedersich, Eds., ASM, Metals Park, OH, (1986).

62. J.H. Perepezko and D.U. Furrer, In Dispersion Strengthened Aluminum Alloys, Y-W. Kim and W.M. Griffith, Eds., TMS, Warrendale, PA, 77 (1988).

63. I.E. Anderson and J.H. Perepezko, In Grain Refinement in Castings and Welds, G.J. Abbaschian, Ed., TMS-AIME, Warrendale, PA, 67 (1983).

64. H.J. Schurhoff, W. Gruhl, and W.G. Burchard, Z. Metallkde., **74**, 132 (1983).

65. H.W. Kerr, J. Cisse, and G.F. Bolling, Acta Met., **22**, 677 (1974).

66. L. Arnberg, L. Backrud, and H. Klang, Met. Tech., 14 (1982).

67. J.L. Murray, Met. Trans., **15A**, 261 (1984).

68. J.H. Perepezko and J.S. Paik, J. Non-Cryst. Solids, **61**, 113 (1984).

69. W. Yoon, J.S. Paik, D. LaCourt and J.H. Perepezko, J. Appl. Phys., **60**, [10], 3489 (1986).

70. B.D. Cullity, Elements of X-Ray Diffraction, Addison-Wesley Pub., 2nd Ed., 137 (1978).

71. L. Kaufman and H. Bernstein, Computer Calculation of Phase Diagrams, Academic Press.

NY, (1970).

72. T.L. Ngai and Y.A. Chang, Calphad, **5**, 267 (1981).

73. T.L. Ngai and Y.A. Chang, Calphad, **6**, 253 (1982).

74. M. Hansen and K. Anderko, Constitution of Binary Alloys, 2nd Ed., McGraw-Hill, New York (1958).

75. W.J. Boettinger and S.R. Coriell, In Science and Technology of the Undercooled Melt: Rapid Solidification Materials and Technologies, NATO ASI Series E, P.R. Sahm, H. Jones and C.M. Adam, Eds., Martinus Nijhoff Pub., Boston, 81 (1986).

76. J.A. Sekhar, M. Mohan, C. Divakar and A.K. Singh, Scripta Met., **18**, 1327 (1984).

77. D. Turnbull, J. Chem. Phys., **20**, 411 (1952).

78. D. Turnbull, Contemp. Phys., **10**, 473 (1969).

79. D. Turnbull, In Prog. Mat. Sci.-Chalmers Ann. Vol., J.W. Christian, P. Haasen and T.B. Massalski, Eds., Pergamon, Oxford 269 (1981).

80. A.S. Skapski, Acta Met., **4**, 576 (1956).

81. F. Spaepen, Acta Met., **23**, 729 (1975).

82. G.E.P. Box, W.G. Hunter, and J.S. Hunter, Statistics for Experimenters, John Wiley, NY (1978).

83. J.S. Paik and J.H. Perepezko, unpublished research.

84. G.R. Wood and A.G. Walton, J. Appl. Phys., **41**, 3027 (1970).

85. J.P. Hirth, Met. Trans., **9A**, 401 (1978).

86. J.H. Perepezko, B.A. Mueller, J.J. Richmond and K.P. Cooper, In Rapidly Quenched Metals, Proc. of the Fifth Int. Conf. on Rapidly Quenched Metals, S. Steeb and H. Warlimont, Eds., Elsevier Sci. Pub., North Holland, NY, 43 (1985).

87. C. Barromee-Gautier, B.C. Giessen, and N.J. Grant, J. Chem. Phys., **48**, 1905 (1968).

TABLE 1: Effect of Processing Parameters on Undercooling

Parameter	Undercooling Response	Remarks
Droplet Size	Increased ΔT with size refinement at constant T	Nucleant isolation follows Poisson statistics
Droplet Coating	Function of coating structure and chemistry; major effect in limiting ΔT	Most effective coating is catalytically inert
Cooling Rate	ΔT generally increases with increasing T	Changing T can alter the nucleation kinetics
Melt Superheat	System specific	Appears to be related to coating catalysis
Composition	T_n follows trend of T_L	Melt purity not usually critical
Pressure	T_n parallels melting curve trend	Change in response can signal alternate phase formation

TABLE 2: Maximum Undercooling Limits

Element	Previous Studies			Current Studies	
	ΔT (°C)	$\Delta T/T_m$	Reference	ΔT (°C)	$\Delta T/T_m$
Al	130	0.14	Turnbull and Cech (1950)	175	0.19
Sb	135	0.15	Turnbull and Cech (1950)	210	0.23
Bi	90	0.16	Turnbull and Cech (1950)	227	0.41
Cd	-	-		110	0.19
Ga	150	0.50	Bosio et al. (1966)	174	0.58
In	-	-		110	0.26
Pb	80	0.13	Turnbull and Cech (1950)	153	0.26
Hg	80	0.34	Turnbull (1952)	88	0.38
Te	-	-		236	0.32
Sn	117	0.23	Pound and LaMer (1952)	191	0.38

TABLE 3.

Summary of Droplet Microstructures

Alloy	Undercooling (^{o}C)	Microstructural Features
Al-Ni		
3wt%Ni	170	Formed supersaturated cells of Al. Precipitation of Al_3Ni observed upon DSC analysis.
6.1wt%Ni	160	Exhibited a multi-zone microstructures which contained 50 -100 nm diameter Al_3Ni particles.
9-12wt%Ni	200	Contained the metastable Al_9Ni_2 phase.
15-19wt%Ni	210	Coupled Al/Al_3Ni morphologies were exhibited.
Al-Fe (hypereutectic)	260	Formation of submicron particles of the metastable Al_6Fe phase.
Al-Fe-Ce (hypereutectic)	320	Suppression of primary Al_3Fe, with a cellular and eutectic structure.
Al-Be (4-15 at%Be)	97	Formation of a finely spaced eutectic (125-150nm) at compositions greater than the eutectic composition.
Al-Y [36] (eutectic)	60	Formation of a submicron dispersoids of Al_3Y in an Al matrix by rapid eutectic growth.
Al-Si [31] (up to 20 wt%Si)	160	Formation of 0.1 to 2.0 micron dispersoids of non-facetted Si in aluminum.

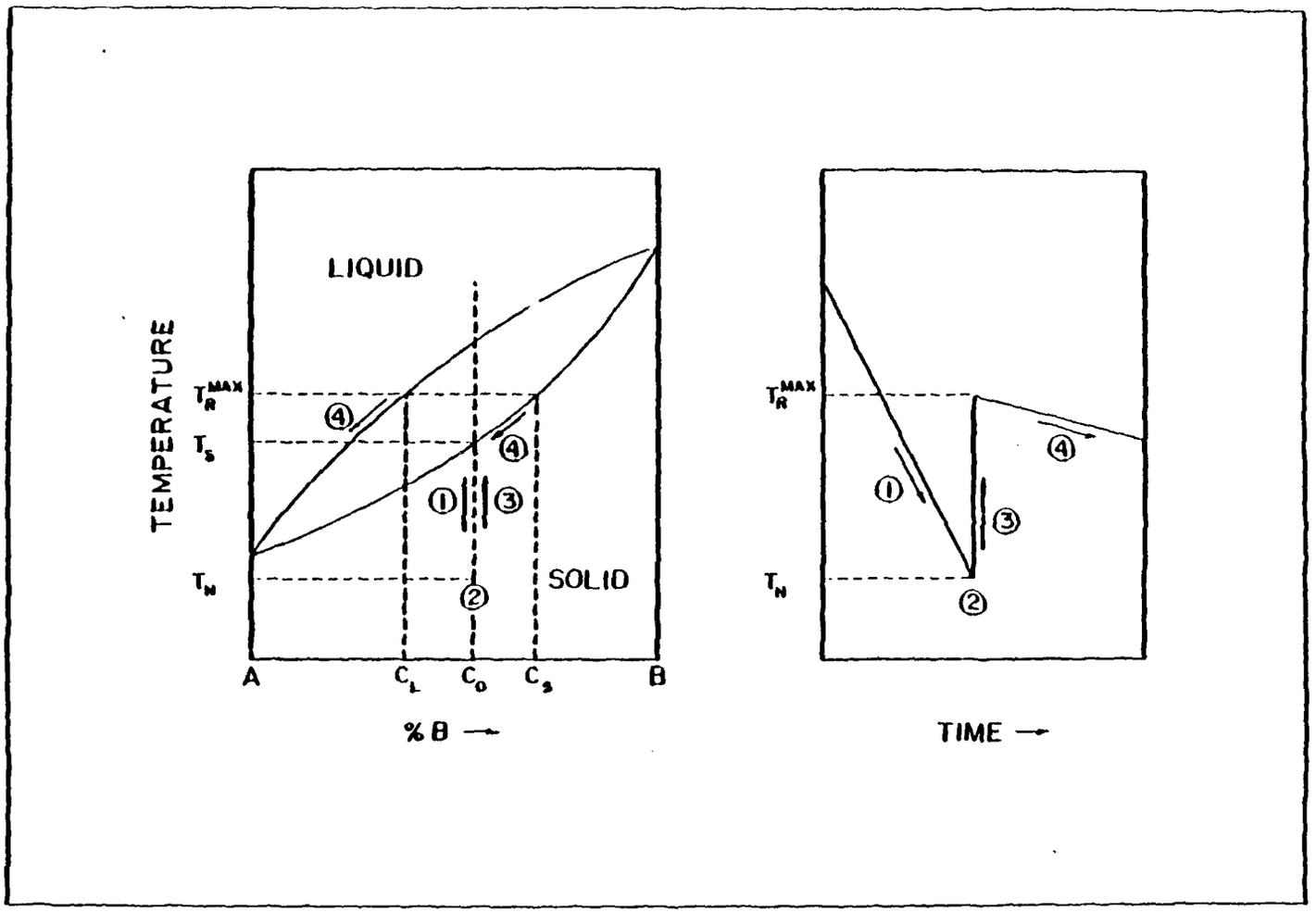

Figure 1. *Schematic representation of the recalescence for an isomorphous alloy of composition C_0.*

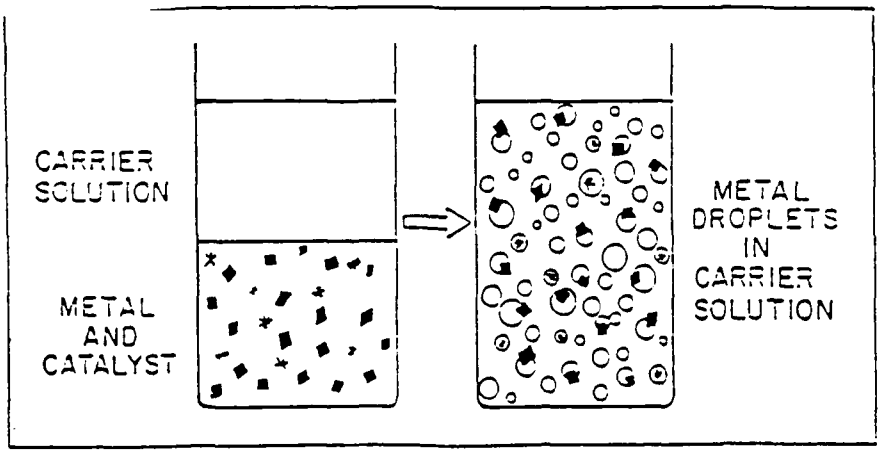

Figure 2. Schematic illustrating nucleant isolation and particle incorporation during droplet emulsification.

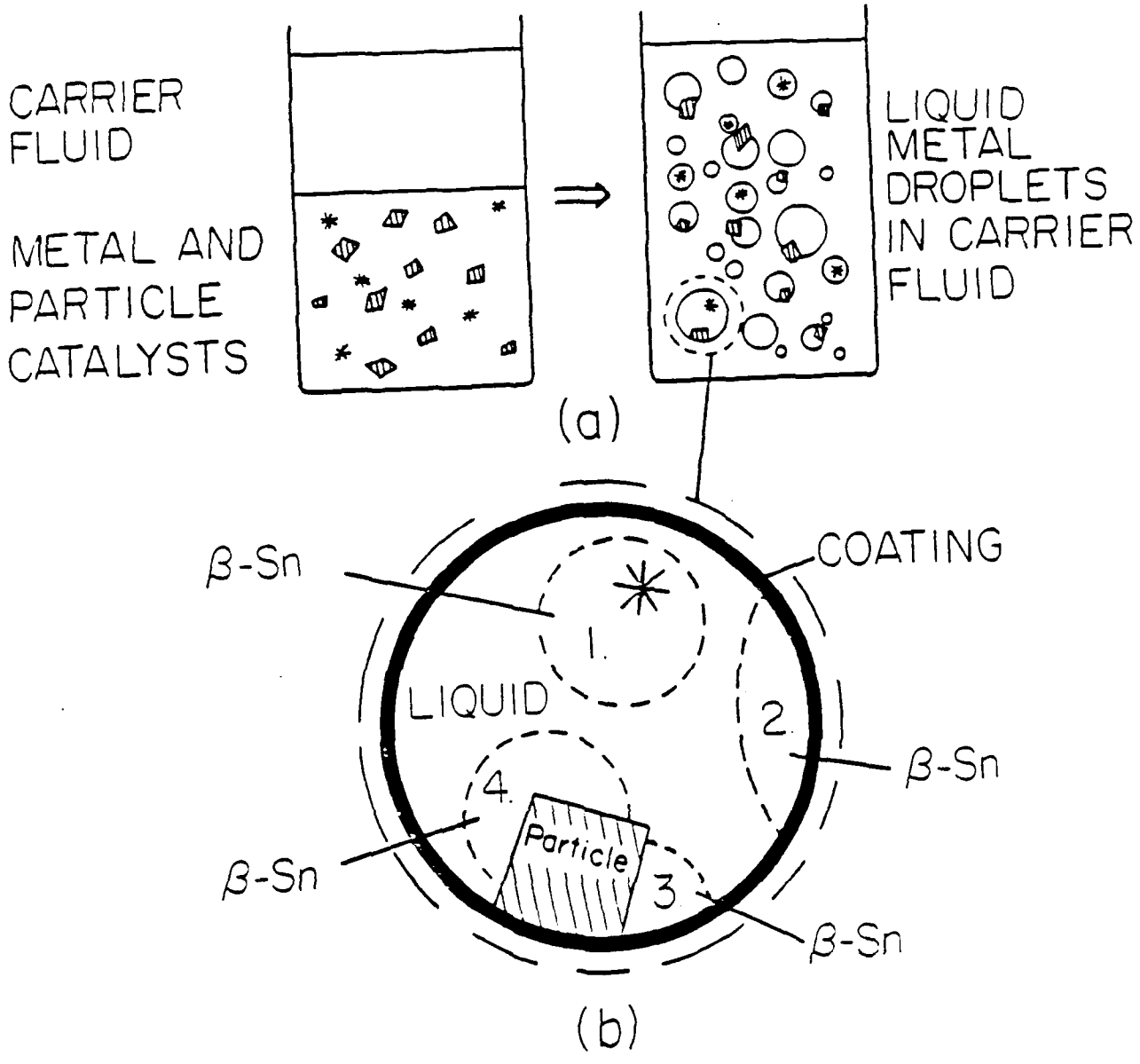

Figure 3. (a) Particle incorporation during droplet emulsification with (b), an enlarged view of a particle incorporated droplet depicting four potential heterogeneous nucleation sites.

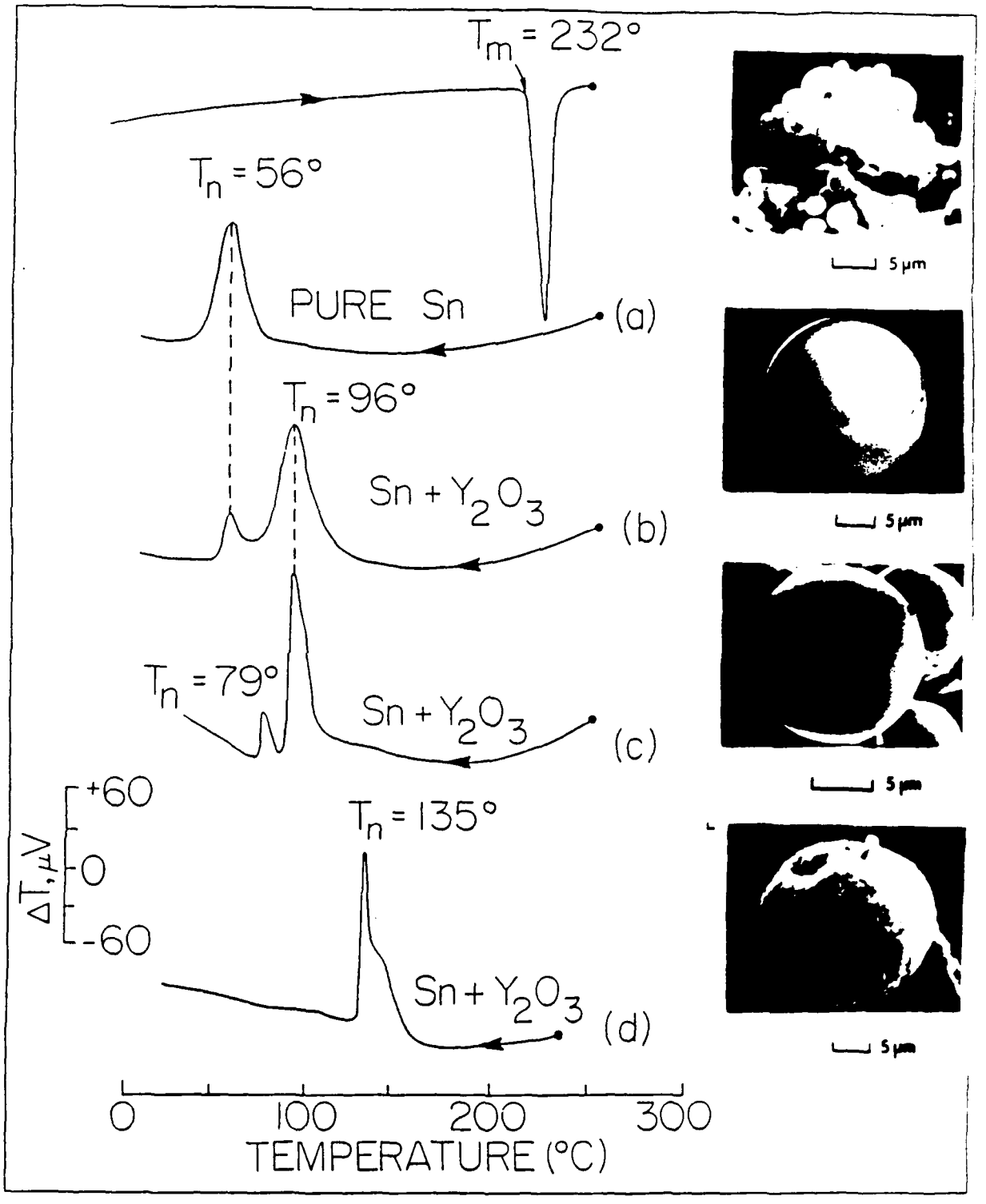

Figure 4. Methodology used for catalytic site identification in particle dispersed droplets as shown in a series of DTA thermograms and accompanying micrographs of pure Sn and Y_2O_3 particle dispersed Sn droplets.

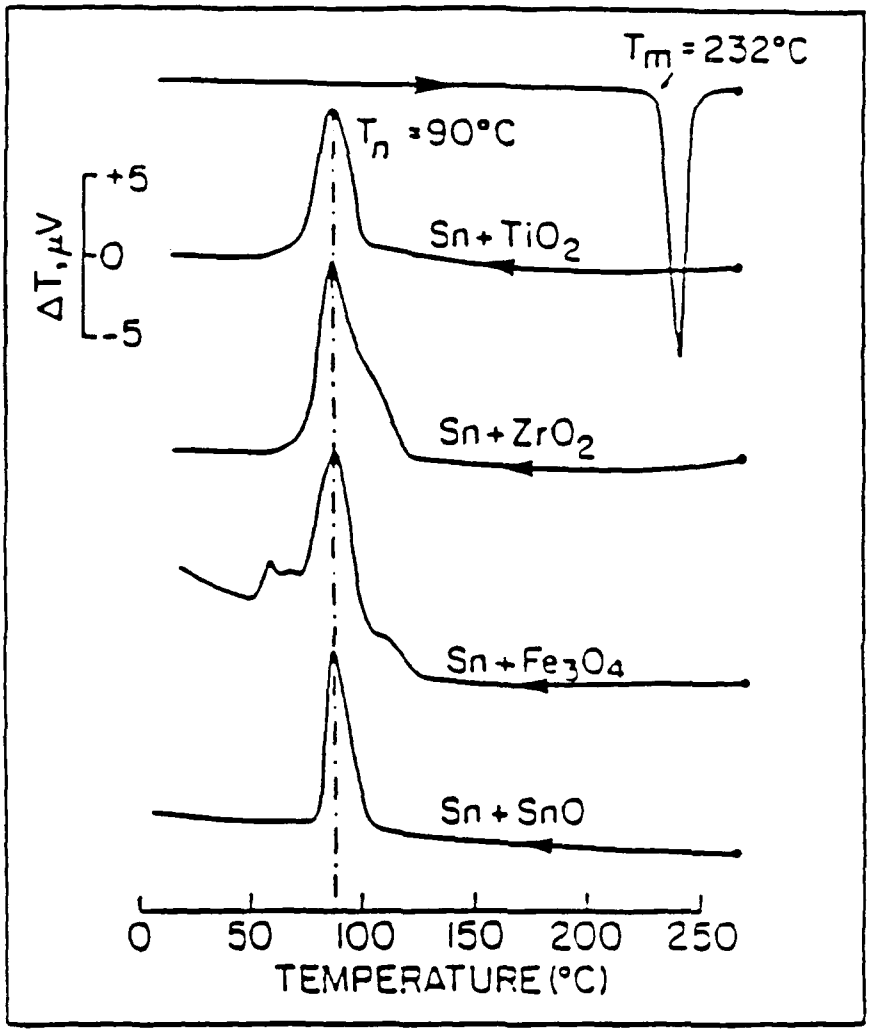

Figure 5. Common undercooling response of Sn droplet emulsions containing different incorporated oxide particles.

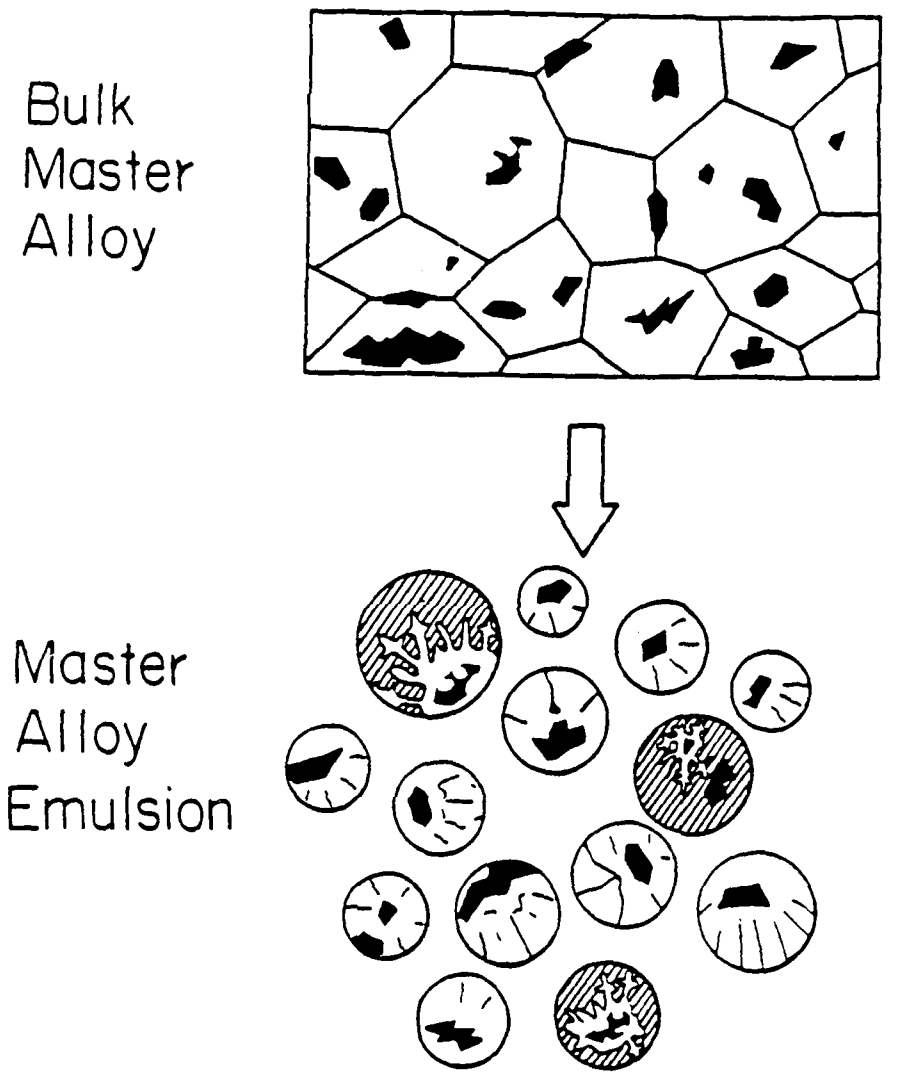

Figure 6. Schematic summarizing the production of Al master alloy powders that contain incorporated inoculant particles of variable effectiveness.

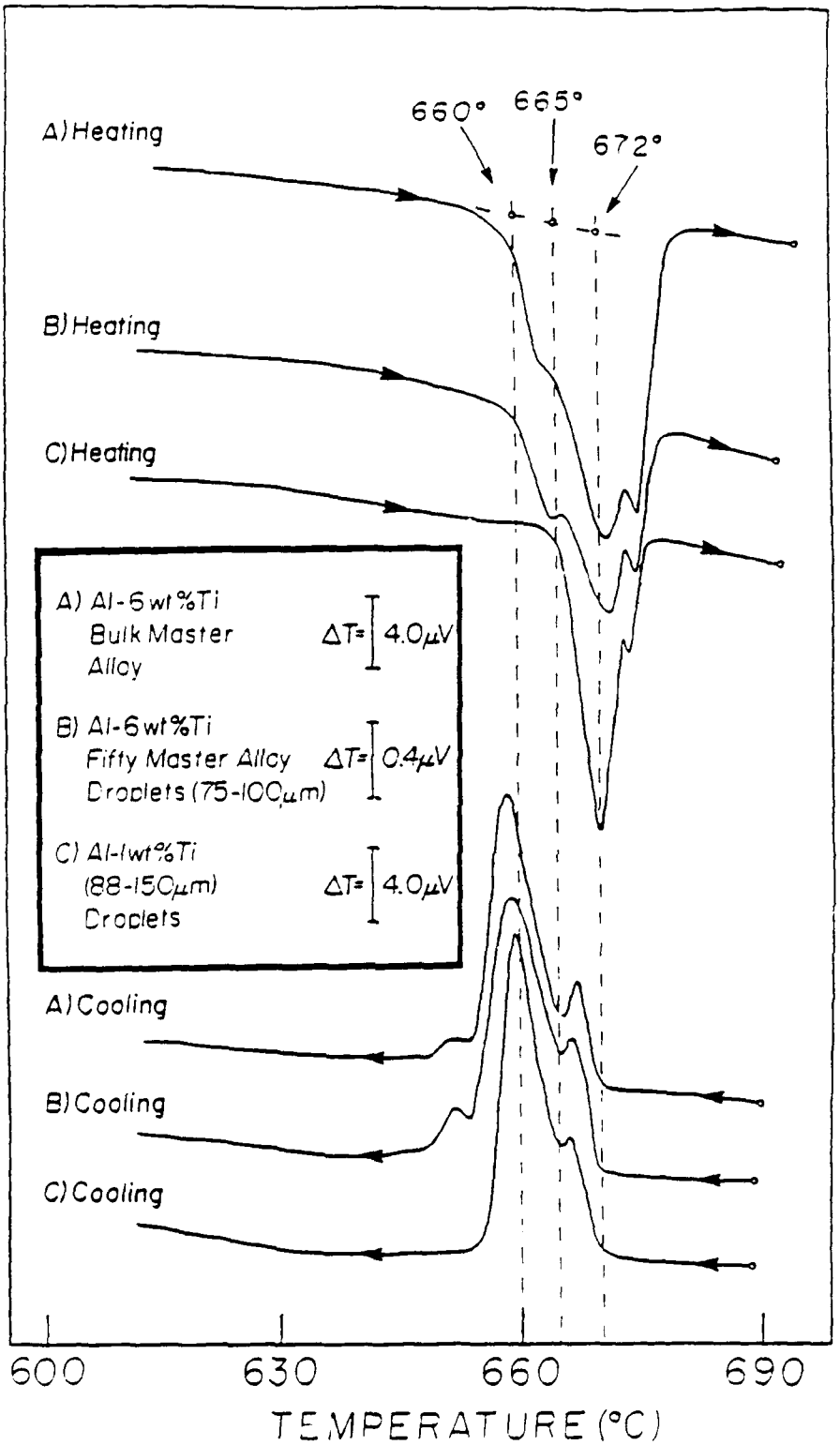

Figure 7. Thermograms Depicting the melting and solidification behavior of; (A) a bulk Al-6 wt% Ti master alloy sample, (B) 75-100μm Al-6 wt% Ti master alloy droplets, and (C) a high purity Al-1 wt% Ti droplet emulsion.

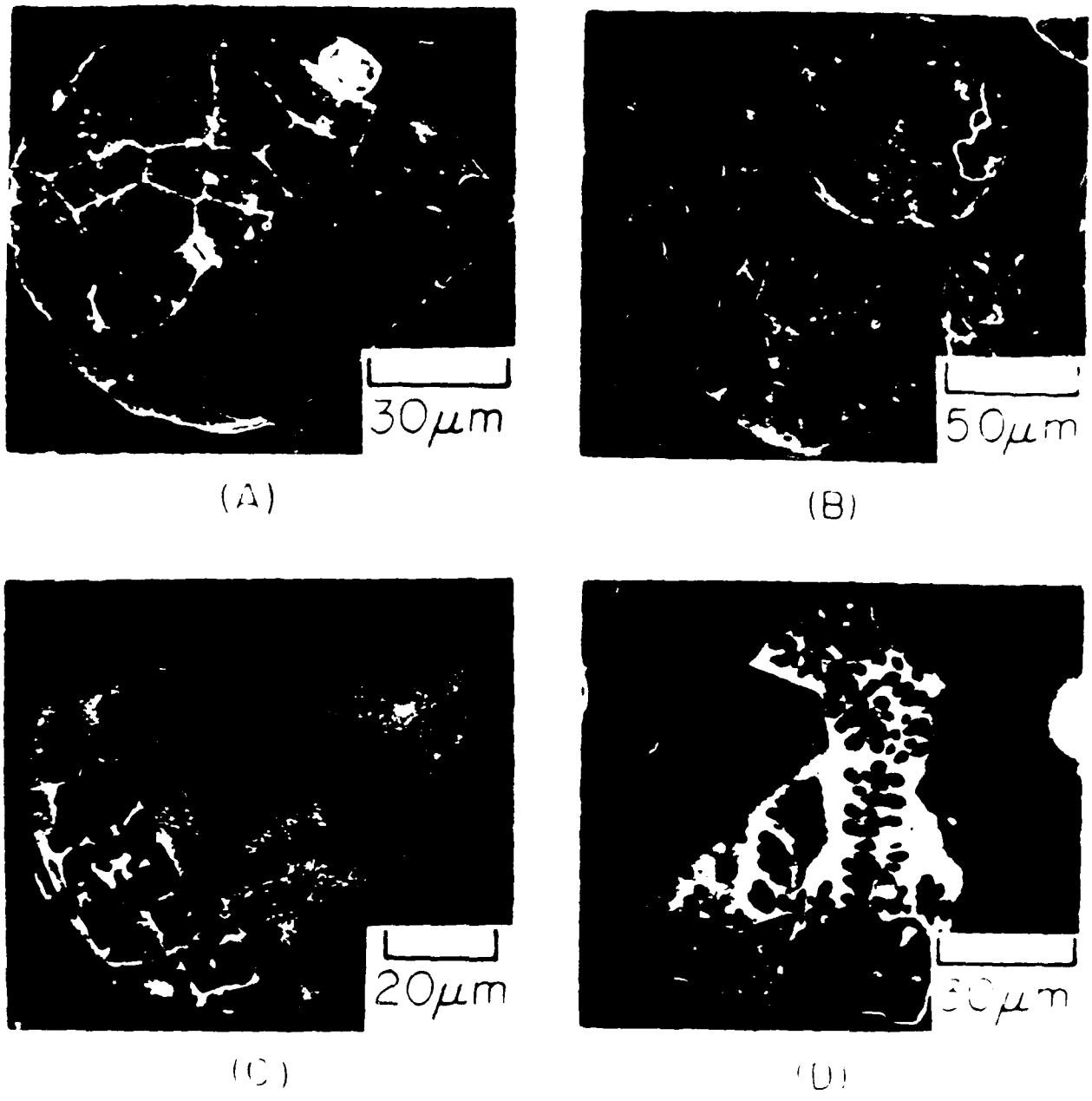

Figure 8. Microstructures produced in Al-6wt% Ti master alloy droplets. A) Large cells produced in a droplet which was still liquid upon quenching from 671°C. B) Cellular microstructures produced from liquid droplets quenched from 700°C. C) Retained dendritic microstructure radiating from an effective inoculant particle which promoted solidification prior to quenching from 671°C. D) Droplet quenched from 671°C exhibiting morphological variances of incorporated effective and ineffective intermetallic particles.

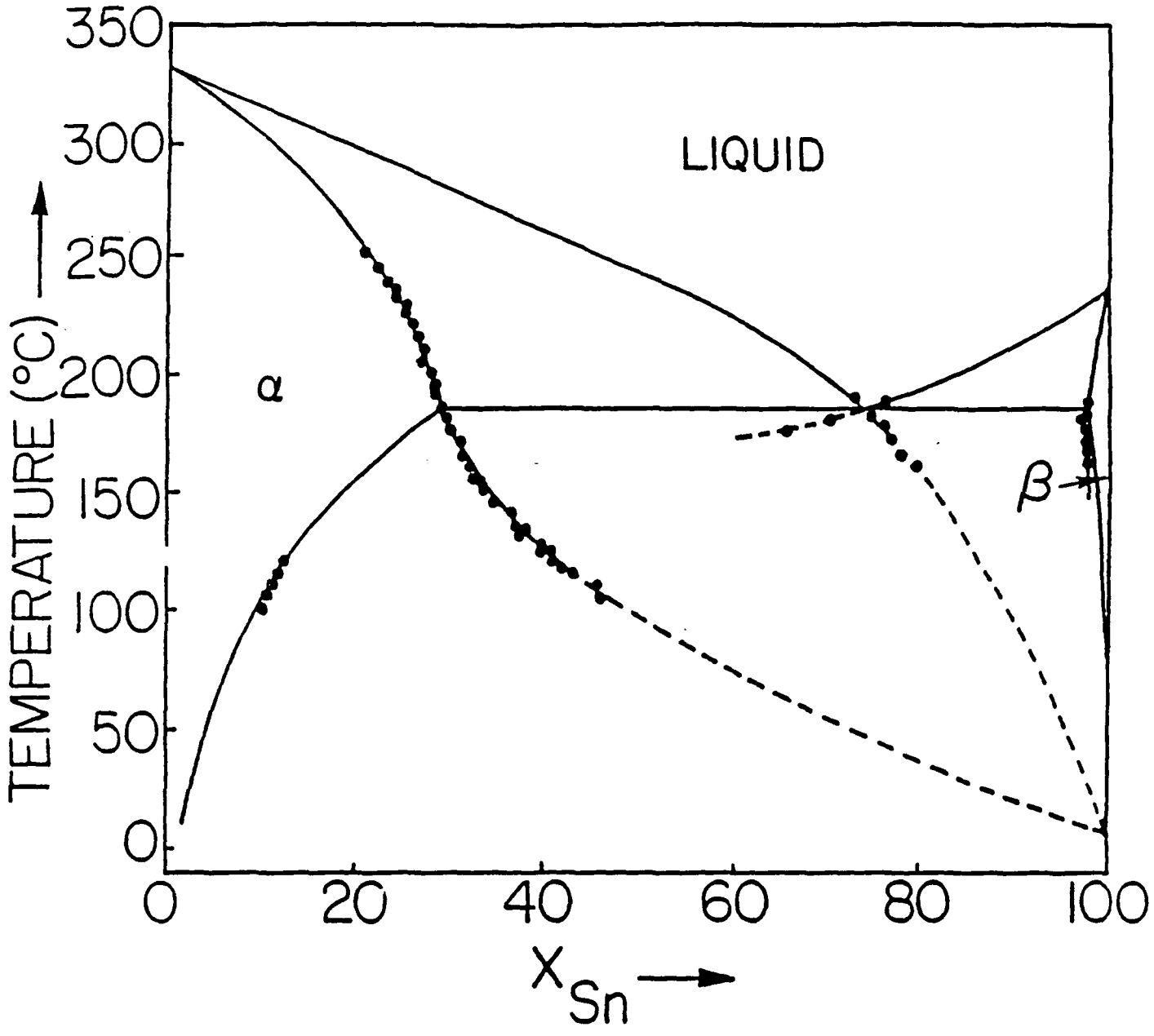

Figure 9. The stable Pb-Sn phase diagram (solid line) including measured and extrapolated extensions (dashed line) of metastable solidus and liquidus.

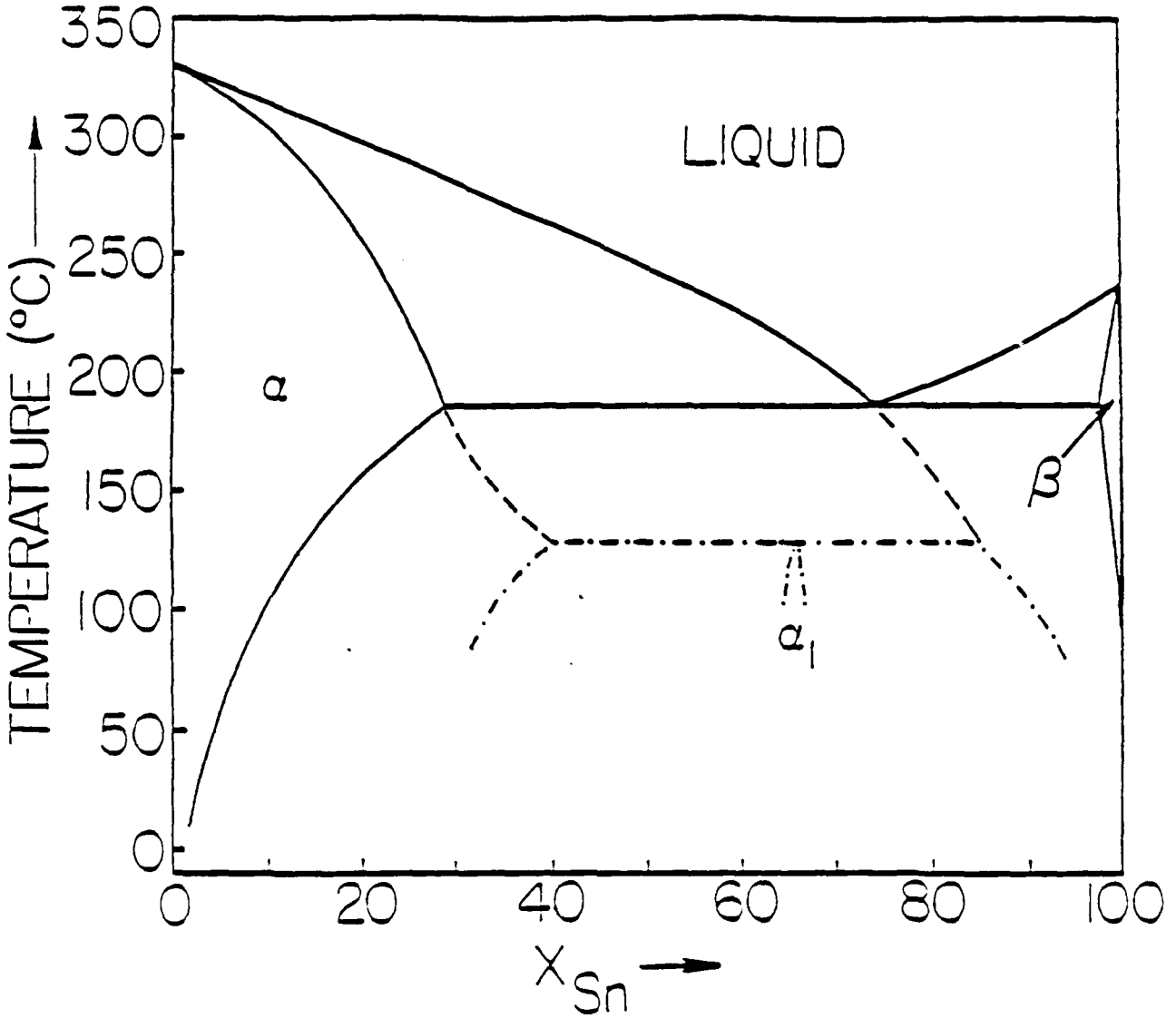

Figure 10. The stable Pb-Sn phase diagram including metastable solidus and liquidus (dashed line) and formation of metastable α_1-phase and related schematic metastable phase boundaries (dash-dotted line).

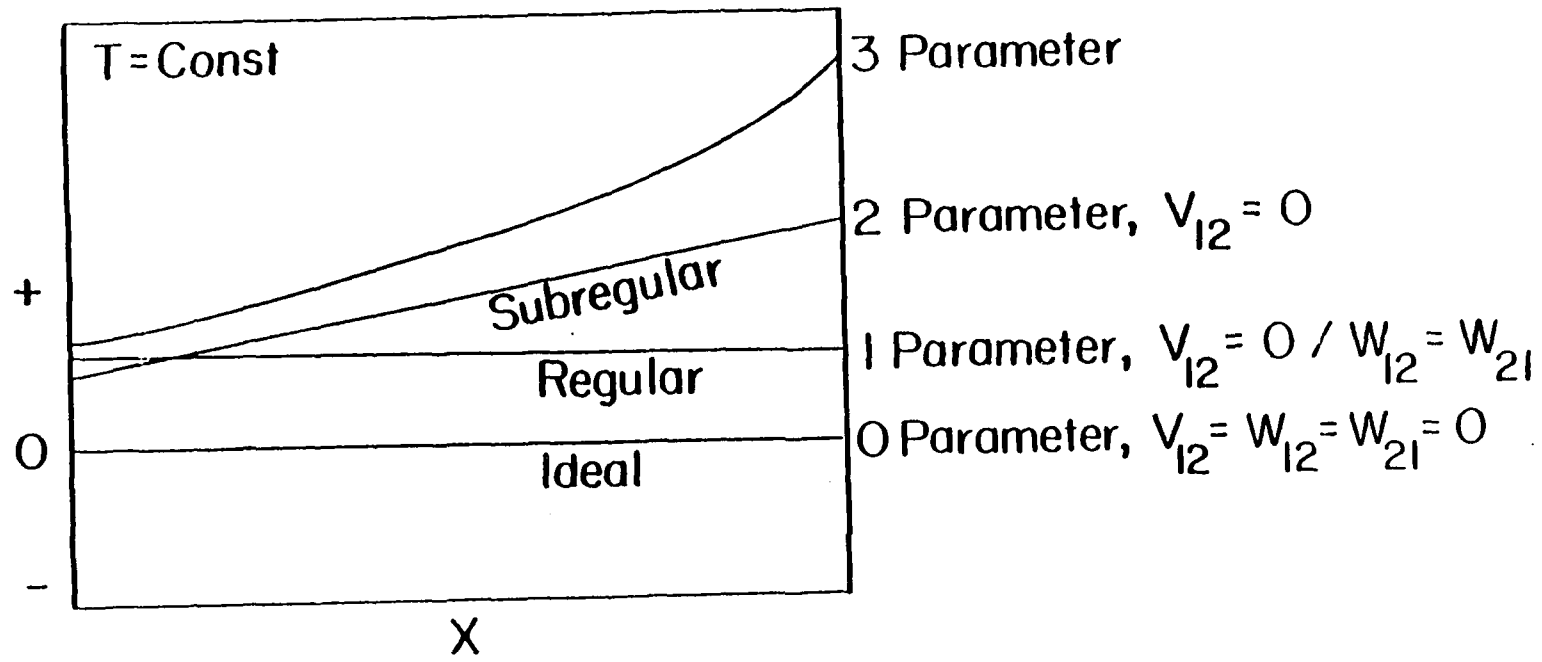

$$\alpha = \frac{\Delta^{XS} \bar{G}^{L}}{(1-X)^2}$$

$$\Delta^{XS} G/RT = 1/2\, X_1 X_2 [(W_{12} + W_{21}) + (W_{12} - W_{21})\ (X_2 - X_1) - 8\, V_{12}^{\alpha} X_1 X_2]$$

Figure 11. **Relationship between ideal, regular, subregular and quasi-subregular solution models.**

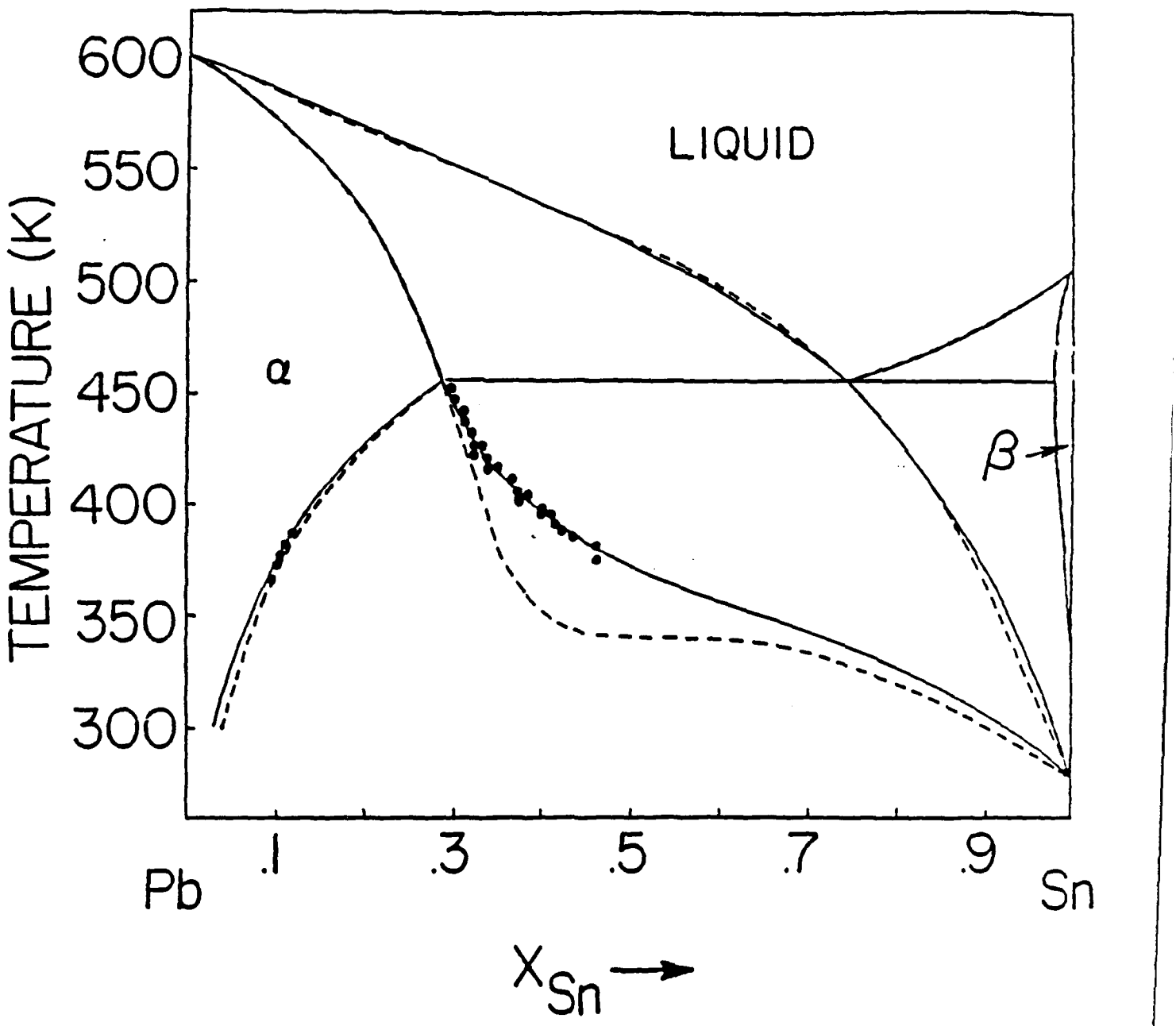

Figure 12. Calculated stable Pb-Sn phase diagram including metastable ($\alpha + L$) extensions applying a quasi-regular (dashed line) or quasi-subregular solution model (solid line).

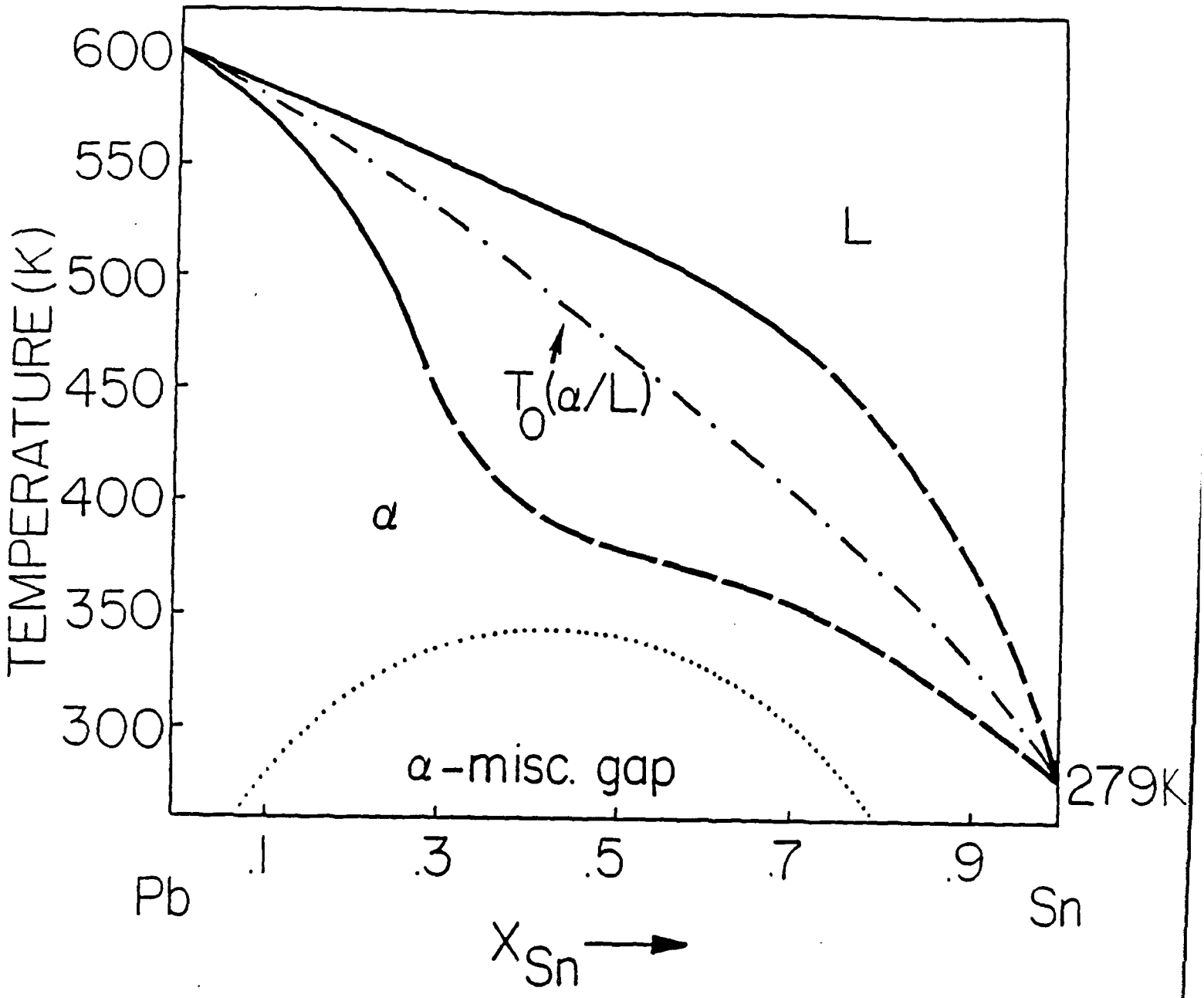

Figure 13. The stable (solid line) and metastable (dashed line) Pb-Sn phase diagram including α and L. The T_0 curve is indicated by the dash-dotted line and the metastable miscibility gap in the α-phase by the dotted line.

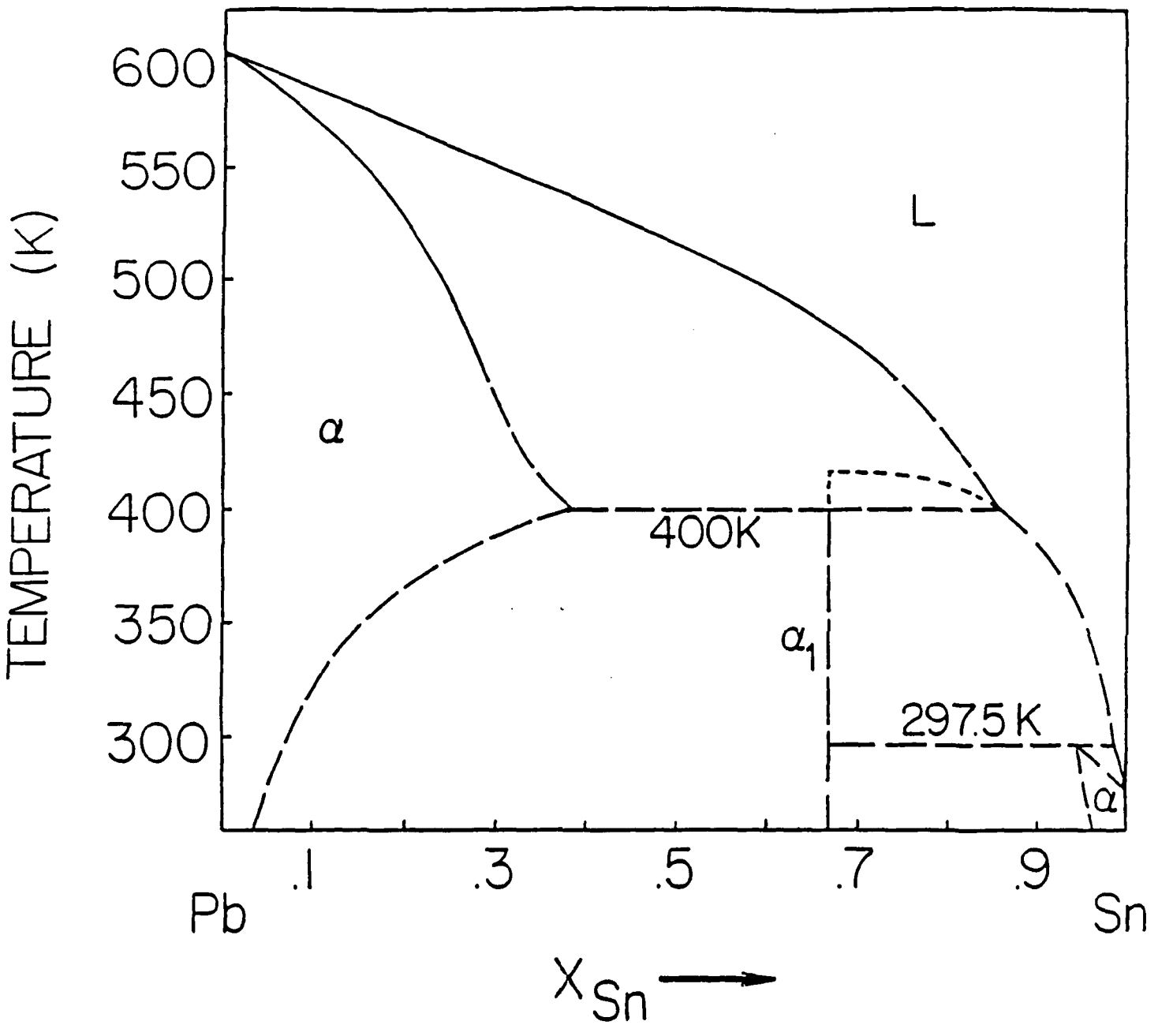

Figure 14. The stable (solid line) and metastable (dashed line) Pb-Sn phase diagram including α, α_1 and L.

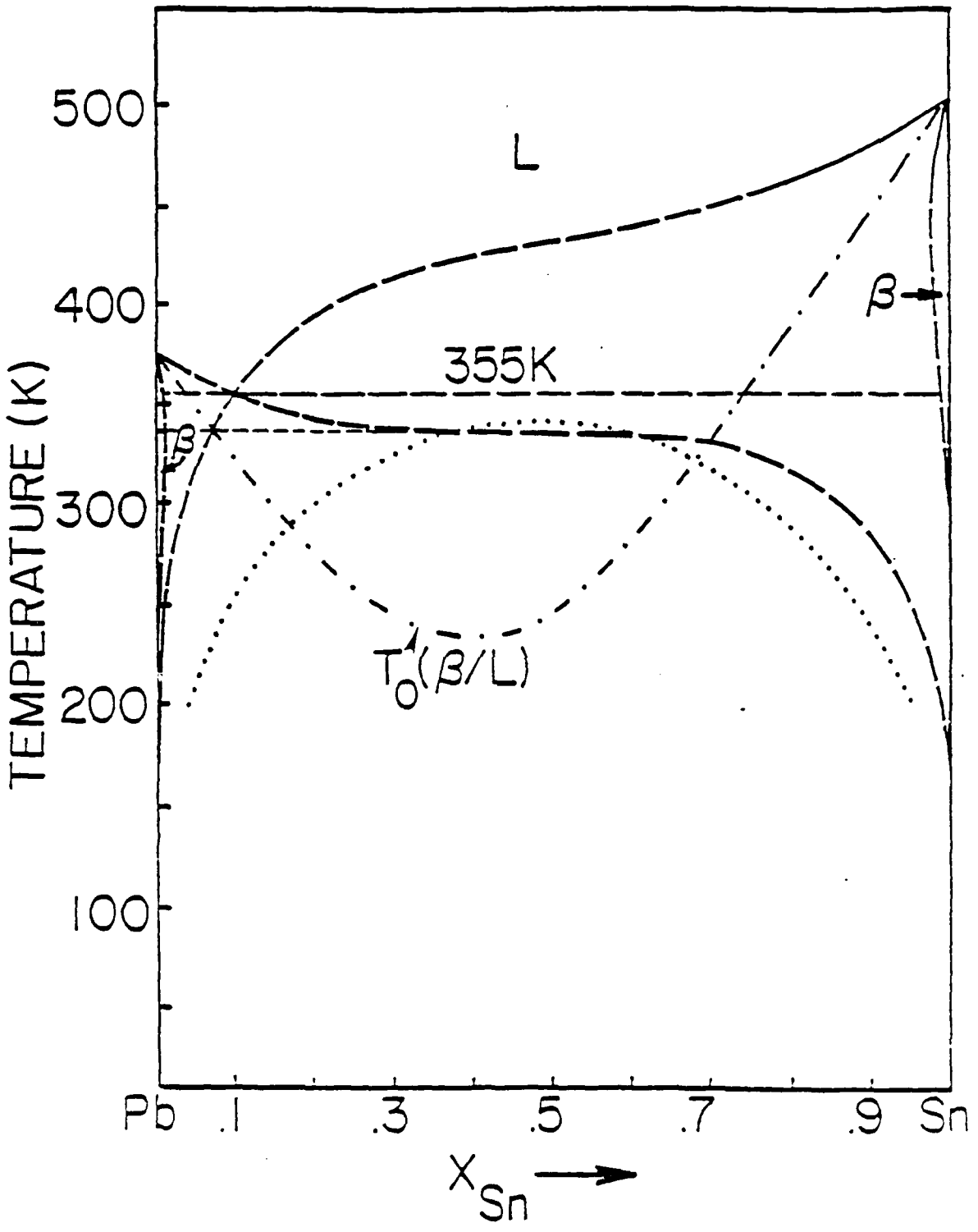

Figure 15. The stable (solid line) and metastable (dashed line) Pb-Sn phase diagram including β and L. The T_0 curve is indicated by the dash-dotted line and the metastable miscibility gap of the undercooled liquid by the dotted line.

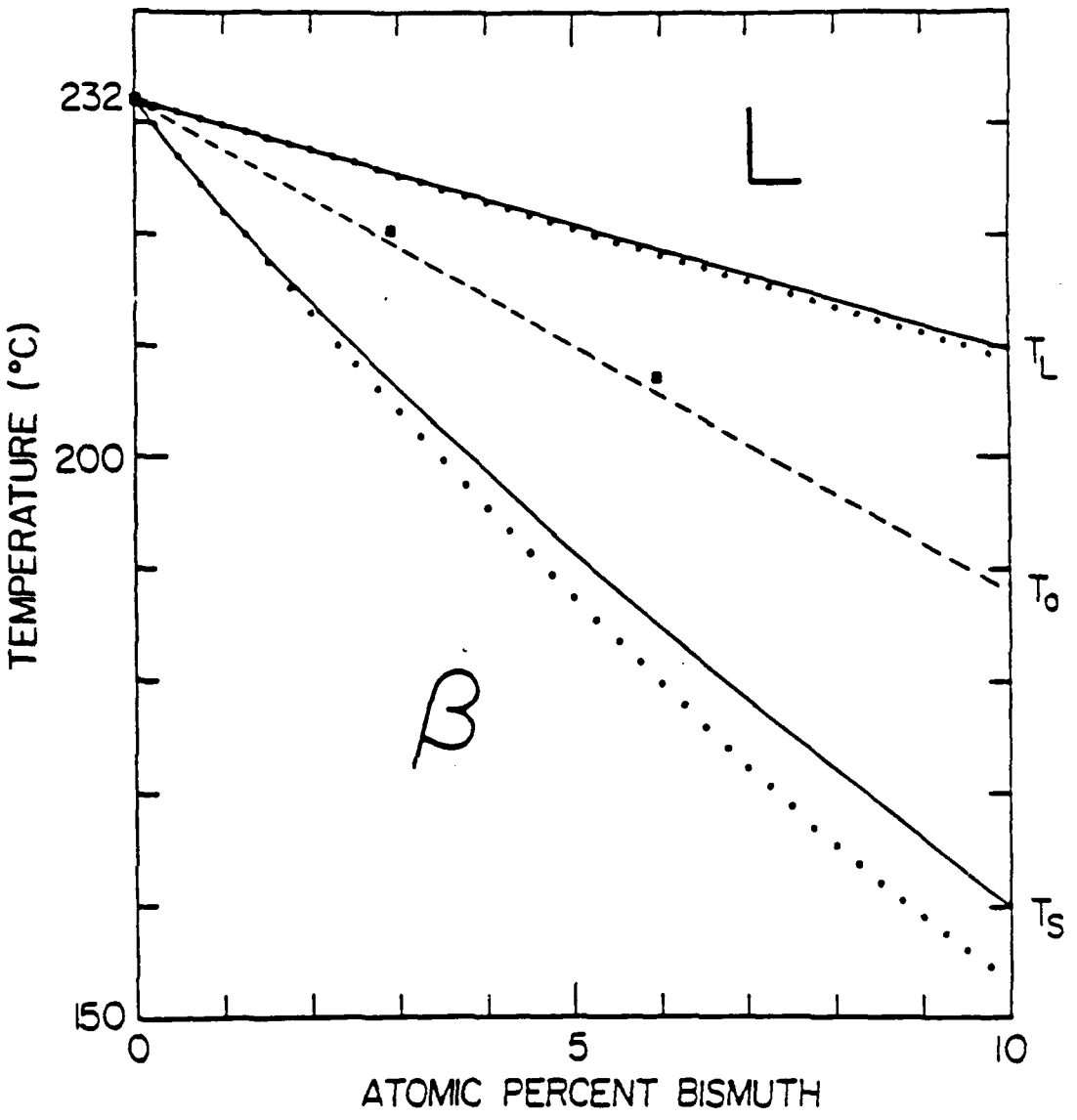

Figure 16. Sn-rich protion of the Sn-Bi phase diagram. Calculated solidus and liquidus are indicated by dotted lines and the calculated T_o curve by the dashed line. The measured temperature of the intermediate melting signal for the two alloys investigated is also indicated.

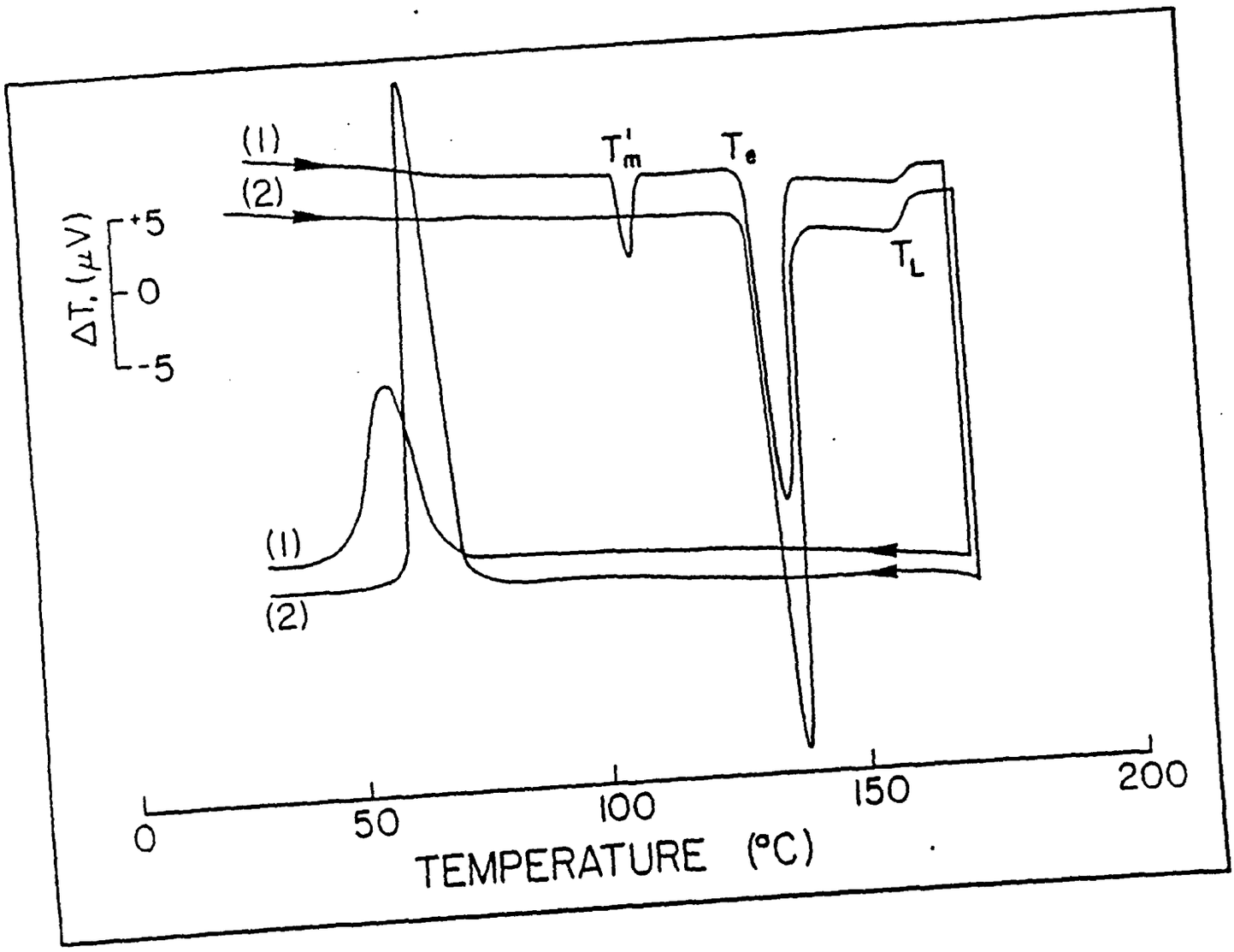

Figure 17. Thermal cycling behavior of a Bi-48.6 at% Sn emulsion at 1 atm. Metastable endothermic behavior appears in a droplet sample with relatively large undercooling.

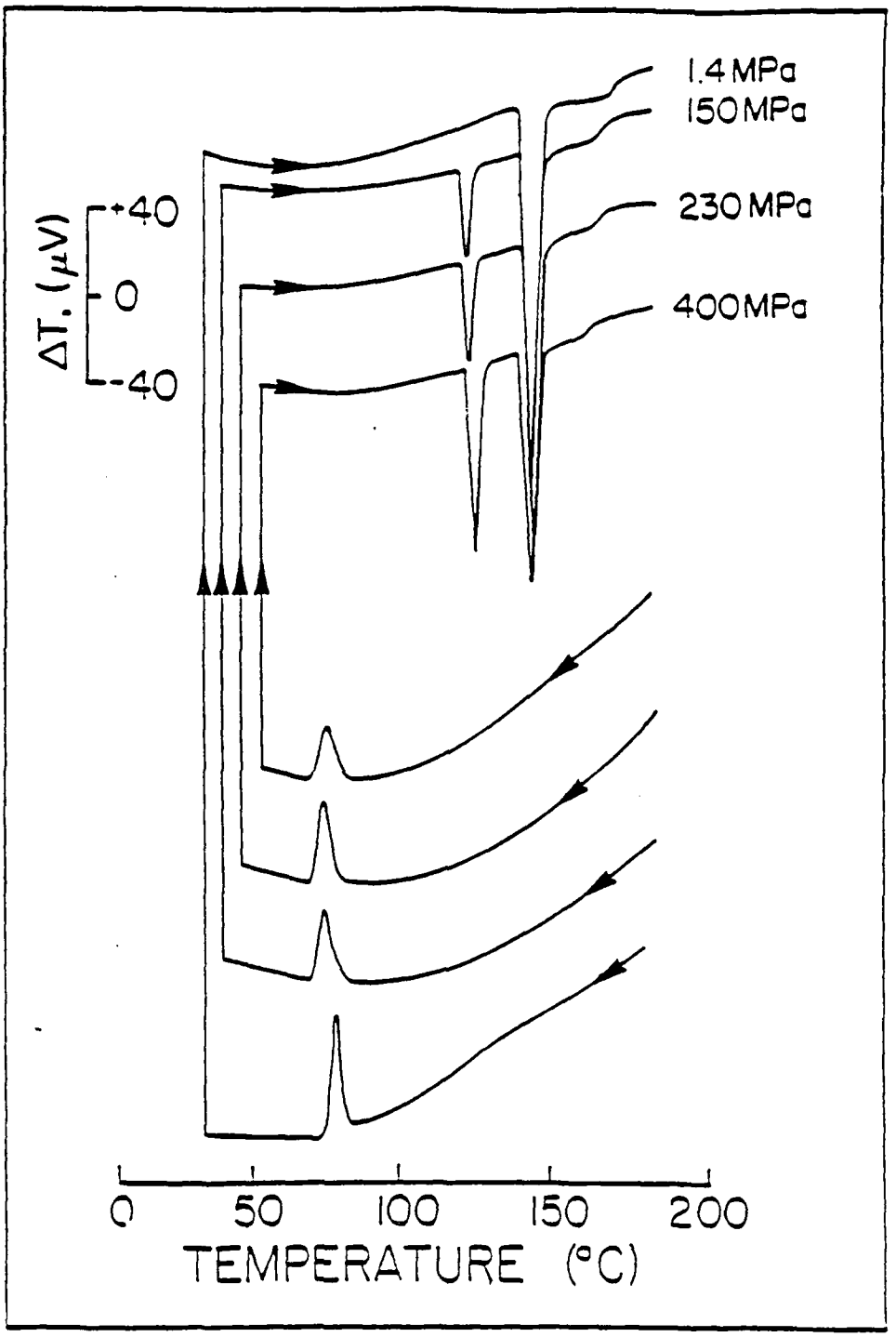

Figure 18. Thermal cycling behavior of a Bi-48.6 at% Sn droplet sample under various pressures where no metastable endothermic behavior appears at ambient pressure.

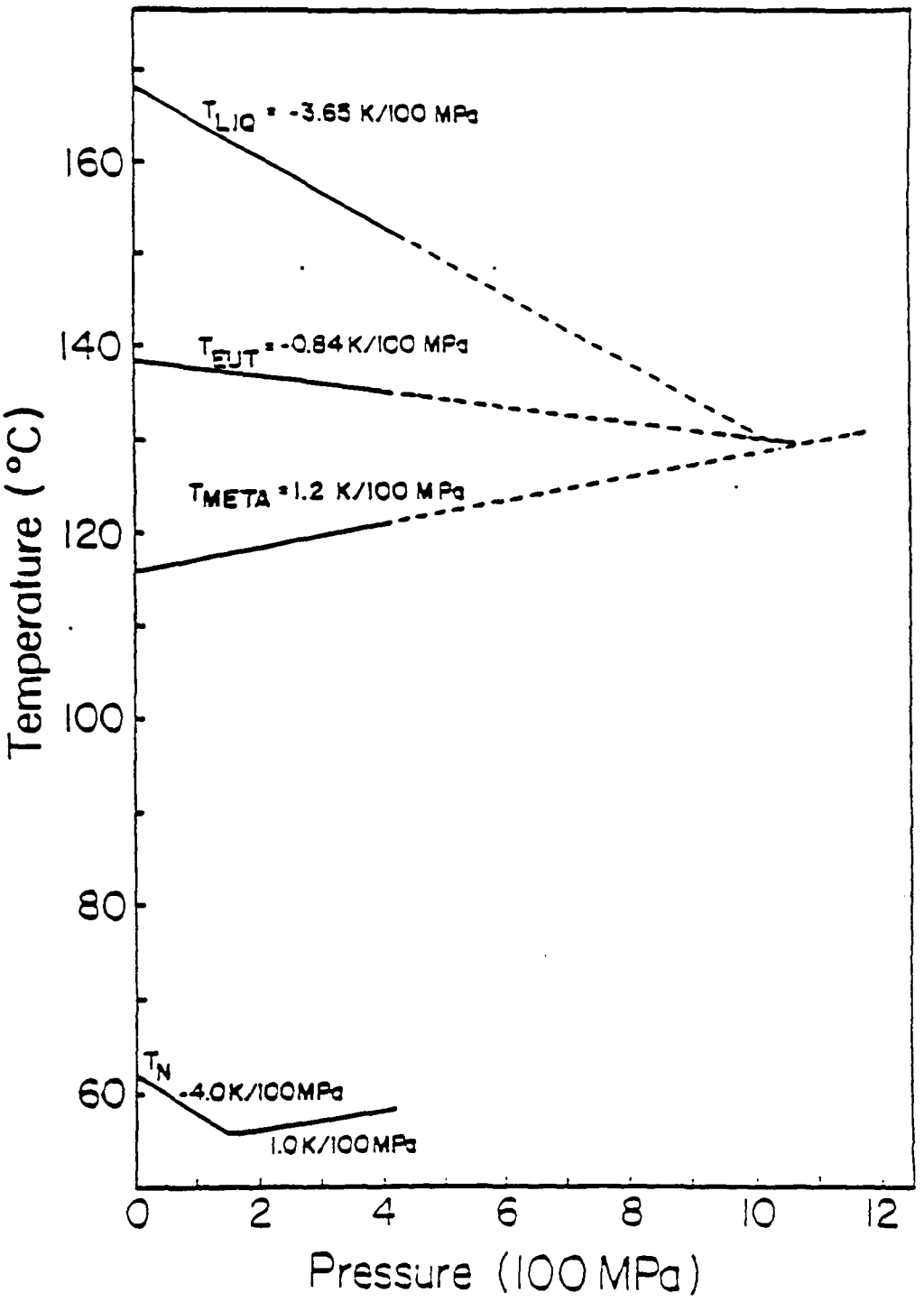

Figure 19. The experimentally observed P-T diagram for a Bi-48.6 at% Sn emulsion sample. Note that the melting temperature of the metastable phase will be higher than that of the eutectic above ~1 GPa; i.e. the metastable phase will be stable above ~1 GPa.

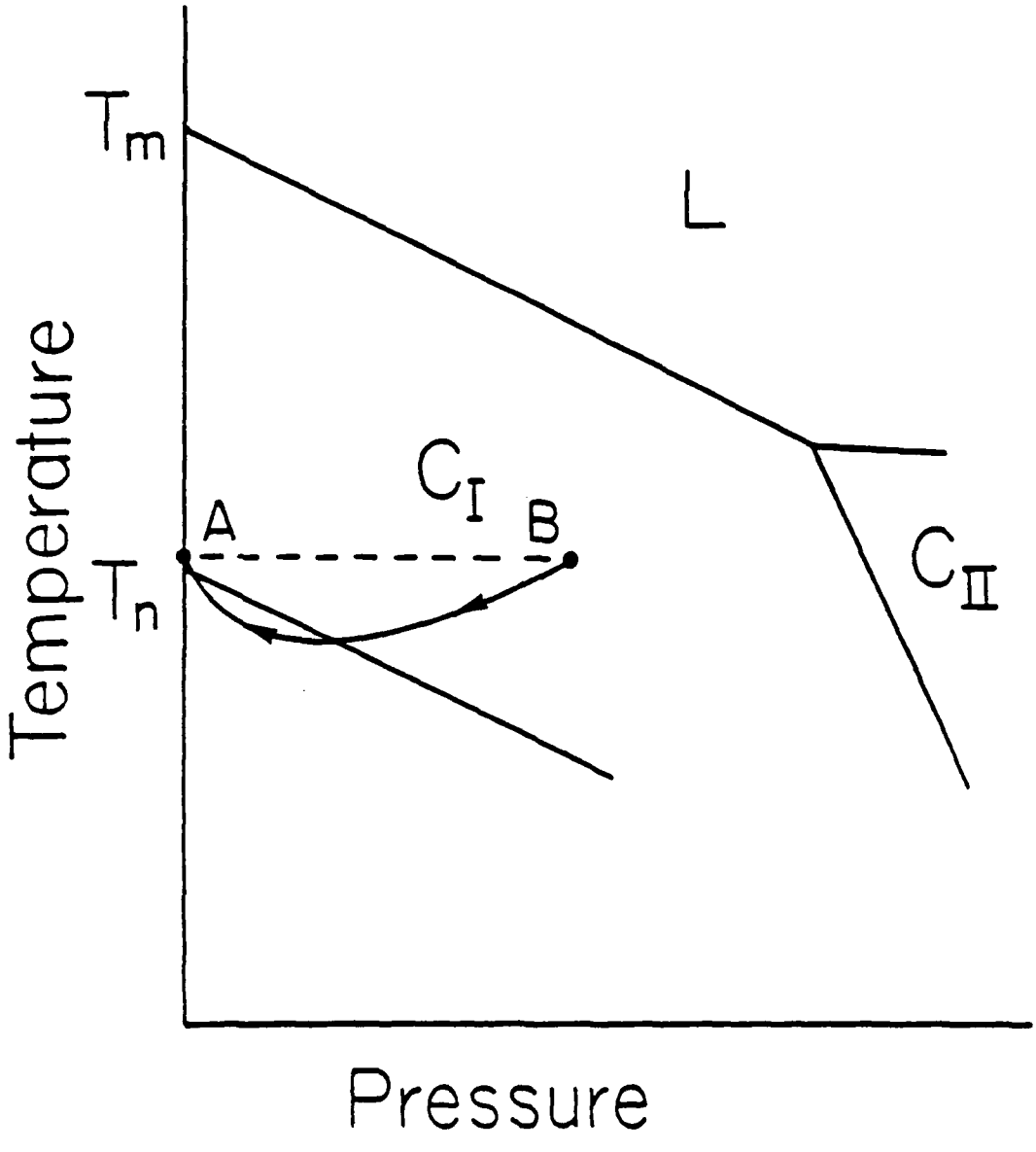

Figure 20. Schematic P-T diagram for an undercooled emulsion sample, $dT_m/dP < 0$.

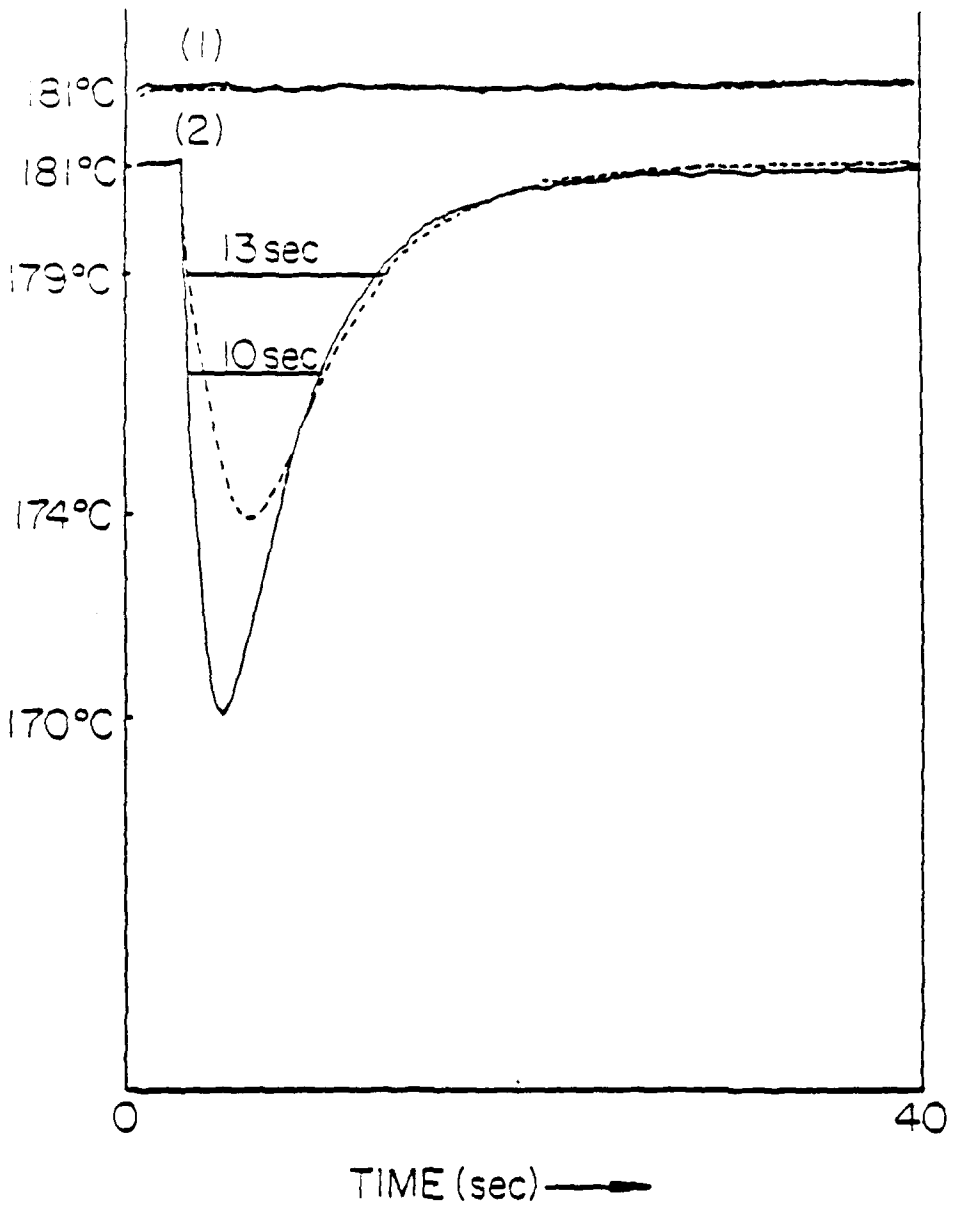

Figure 21. Oscillograms recorded during rapid pressure quench (pure Bi).

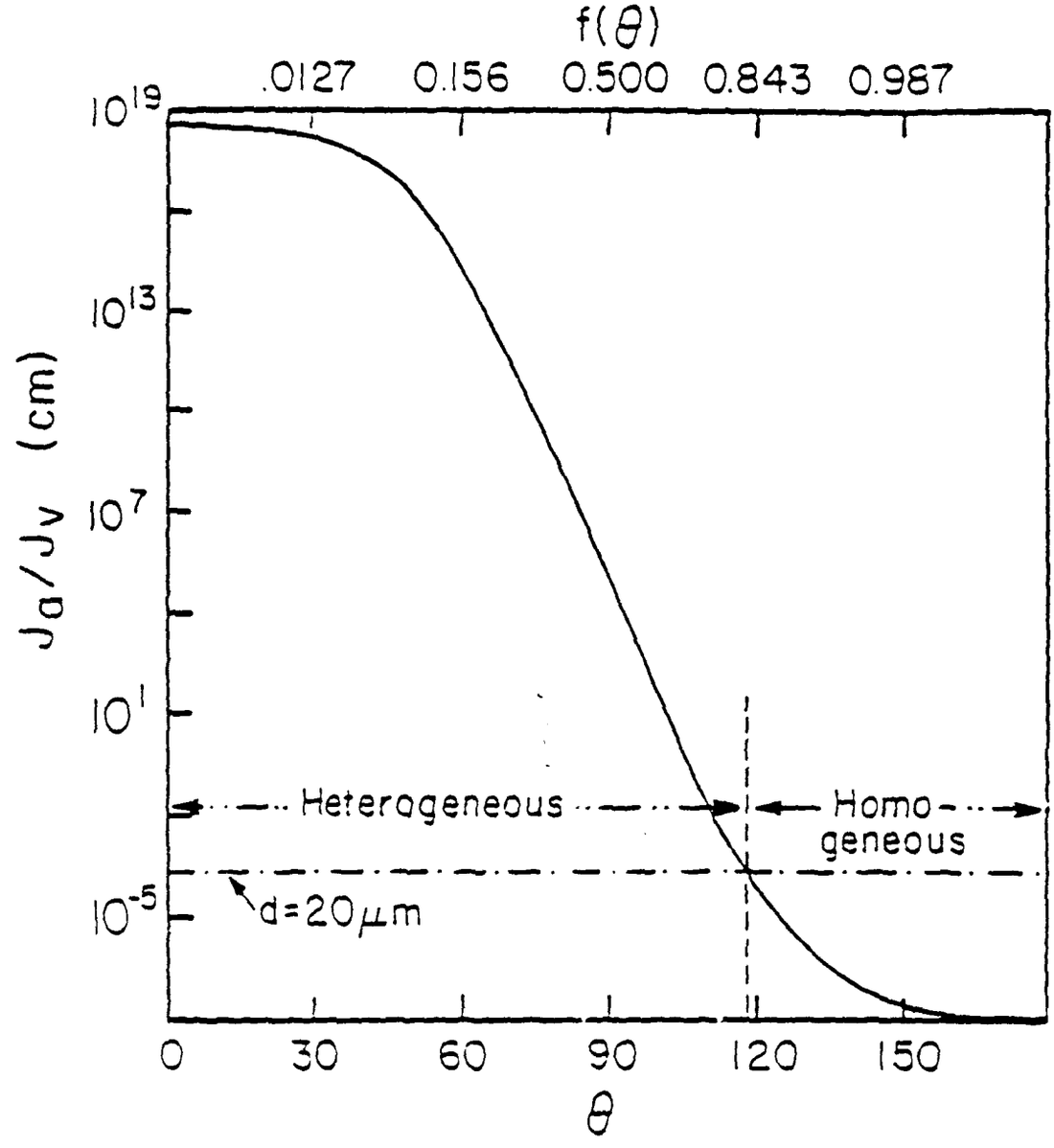

Figure 22. Relative magnitudes of heterogeneous surface to homogeneous nucleation in a 20 μm droplet as a function of contact angle.

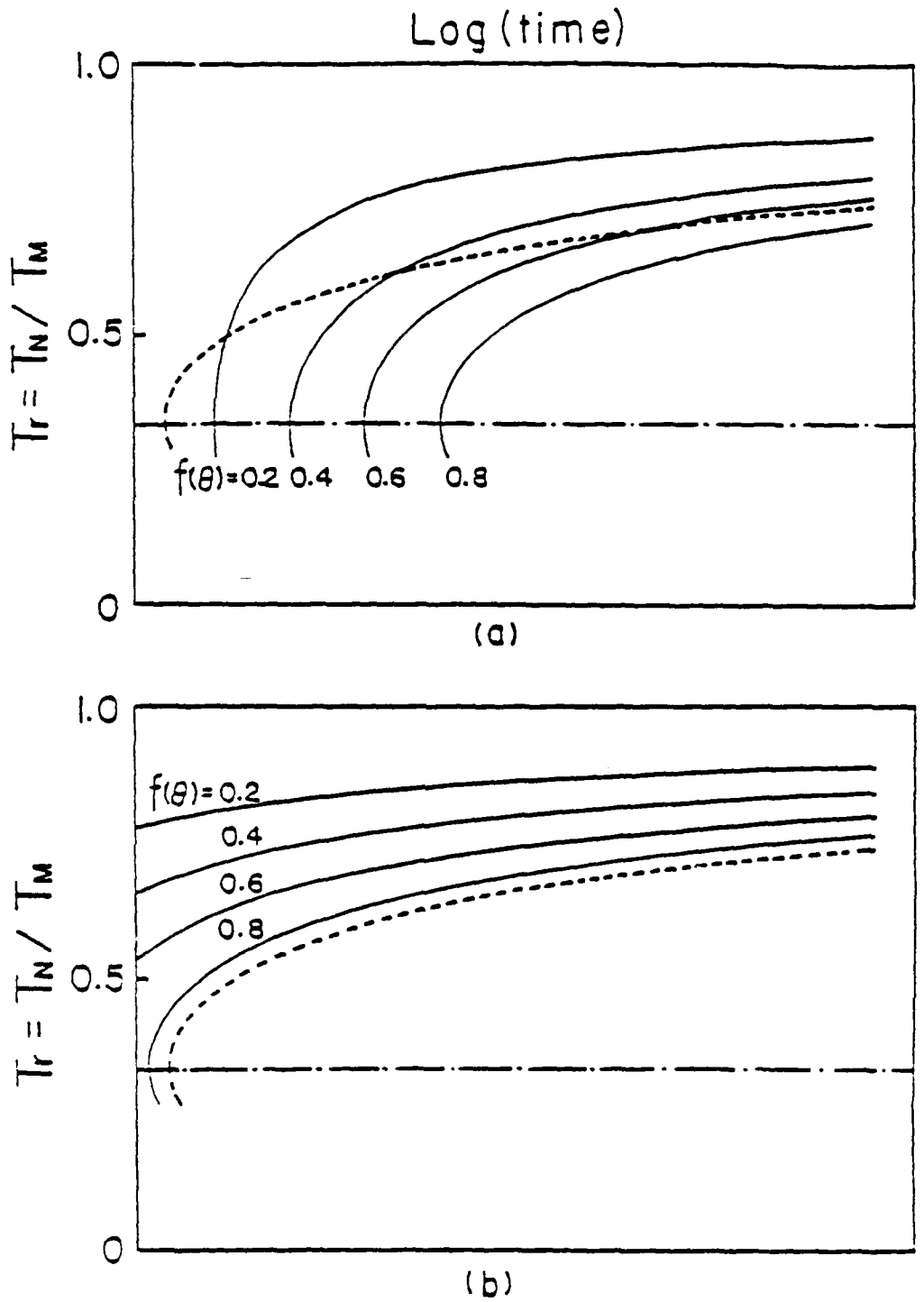

Figure 23. Time-Temperature-transformation diagram representation of the transitions in nucleation kinetics that may occur in undercooled liquids.

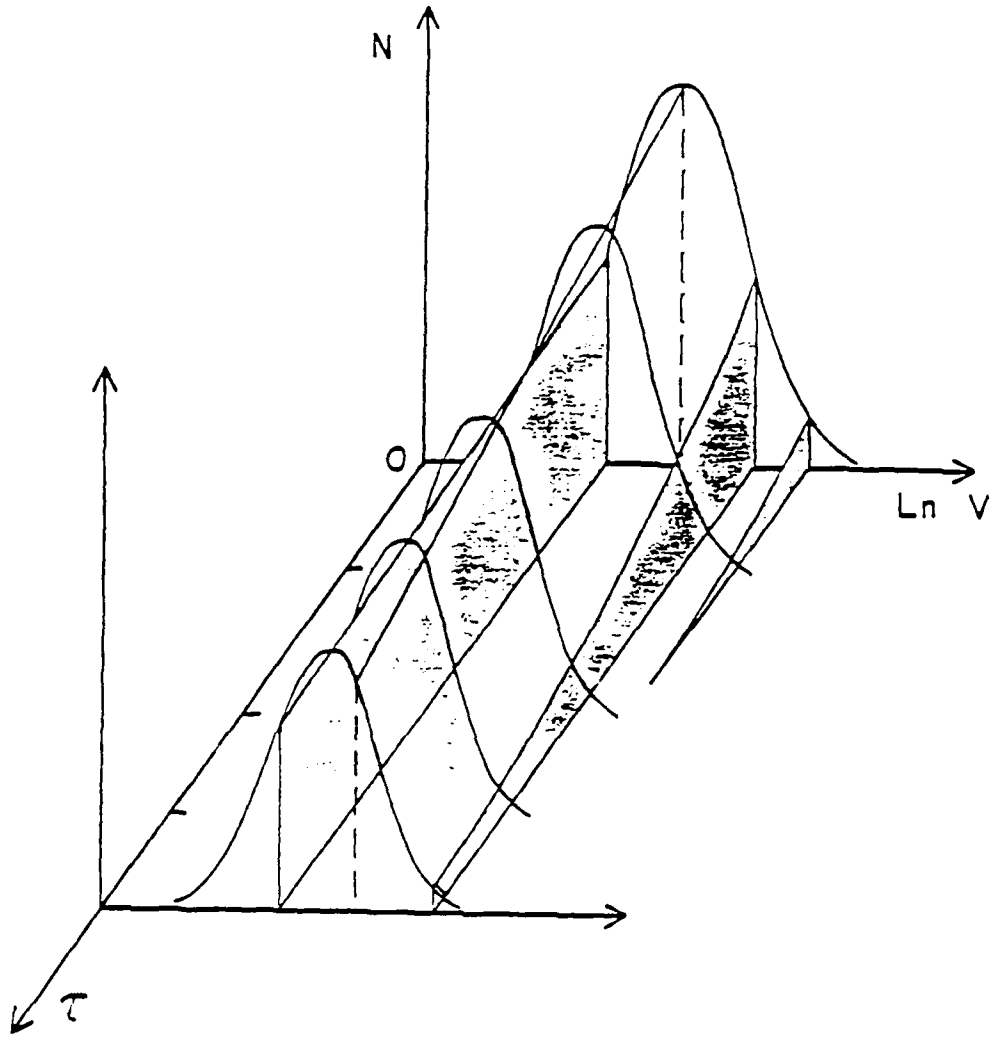

Figure 24. Illustration of the decay of the number of unfrozen droplets during isothermal nucleation at different intervals of $\tau = J_v t$ for a volume dependent process.

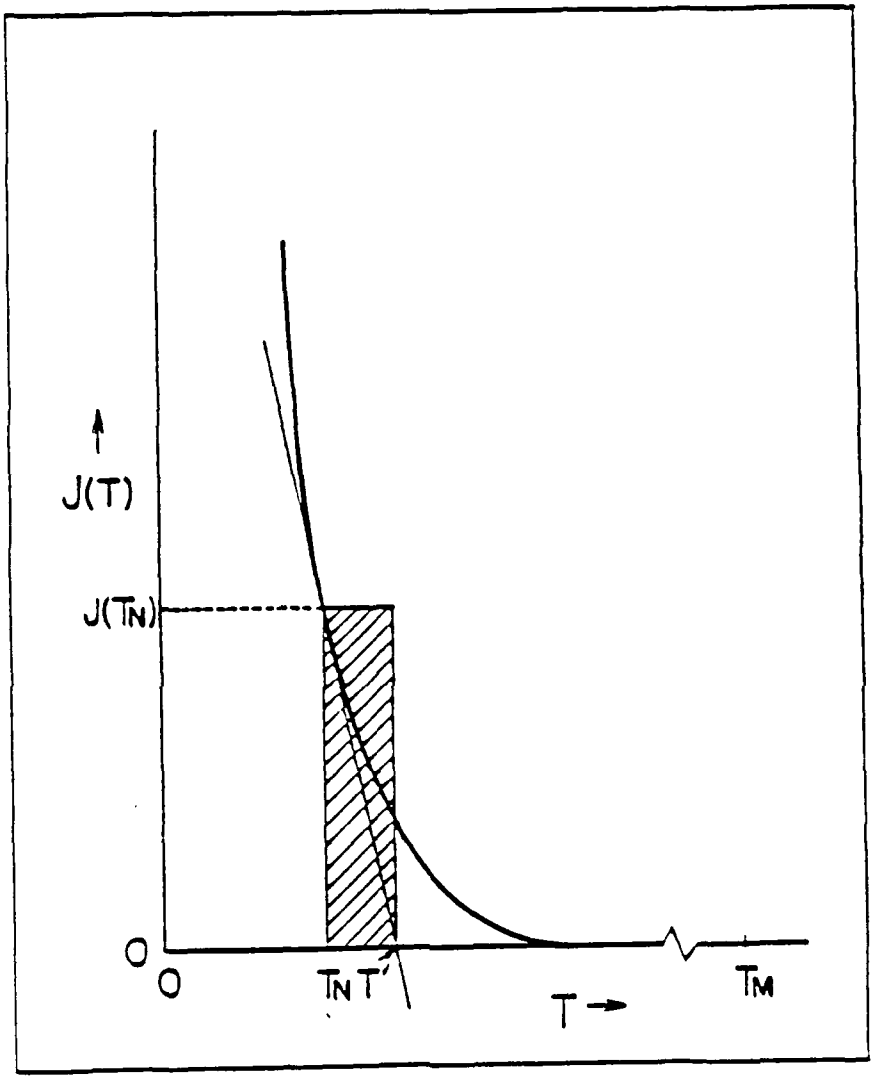

Figure 25. Graphical representation of the approximate evaluation of droplet nucleation during continuous cooling.

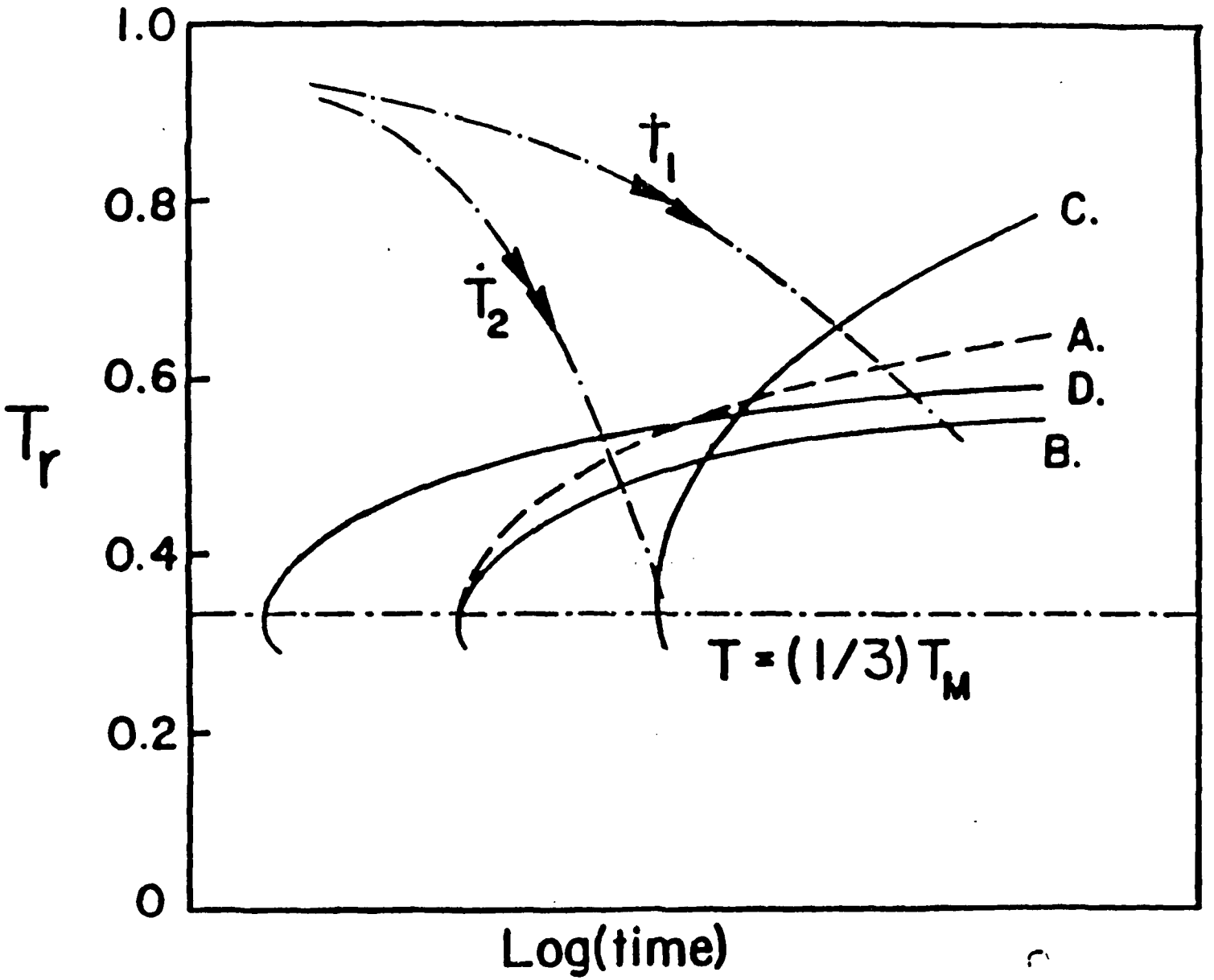

Figure 26. Transformation diagram representing different nucleation kinetics that may occur during continuous cooling of undercooled liquids.

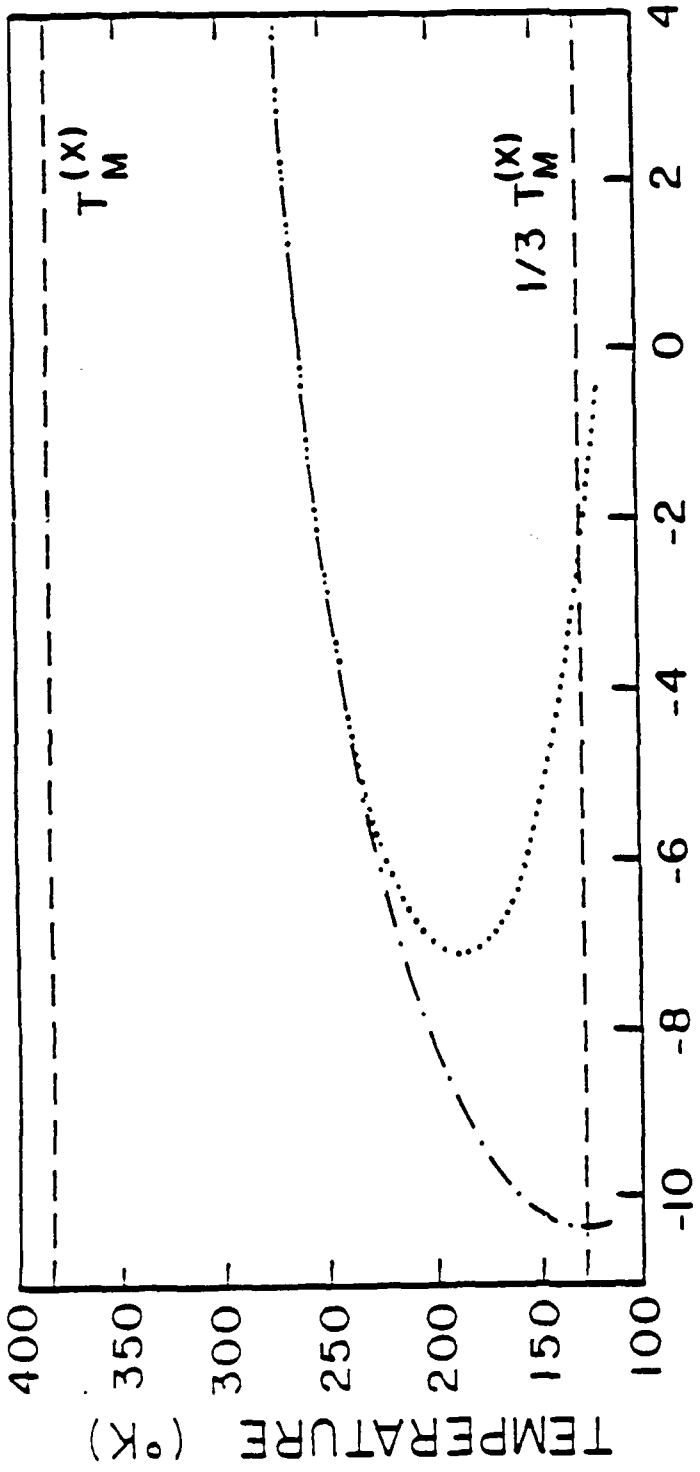

Figure 27. Calculated heterogeneous nucleation kinetics for x-phase in Pb-56 at% Bi droplets. The dotted curve is based on measured ΔG_v and the dotted and dashed curve is derived from the linear ΔG_v approximation.

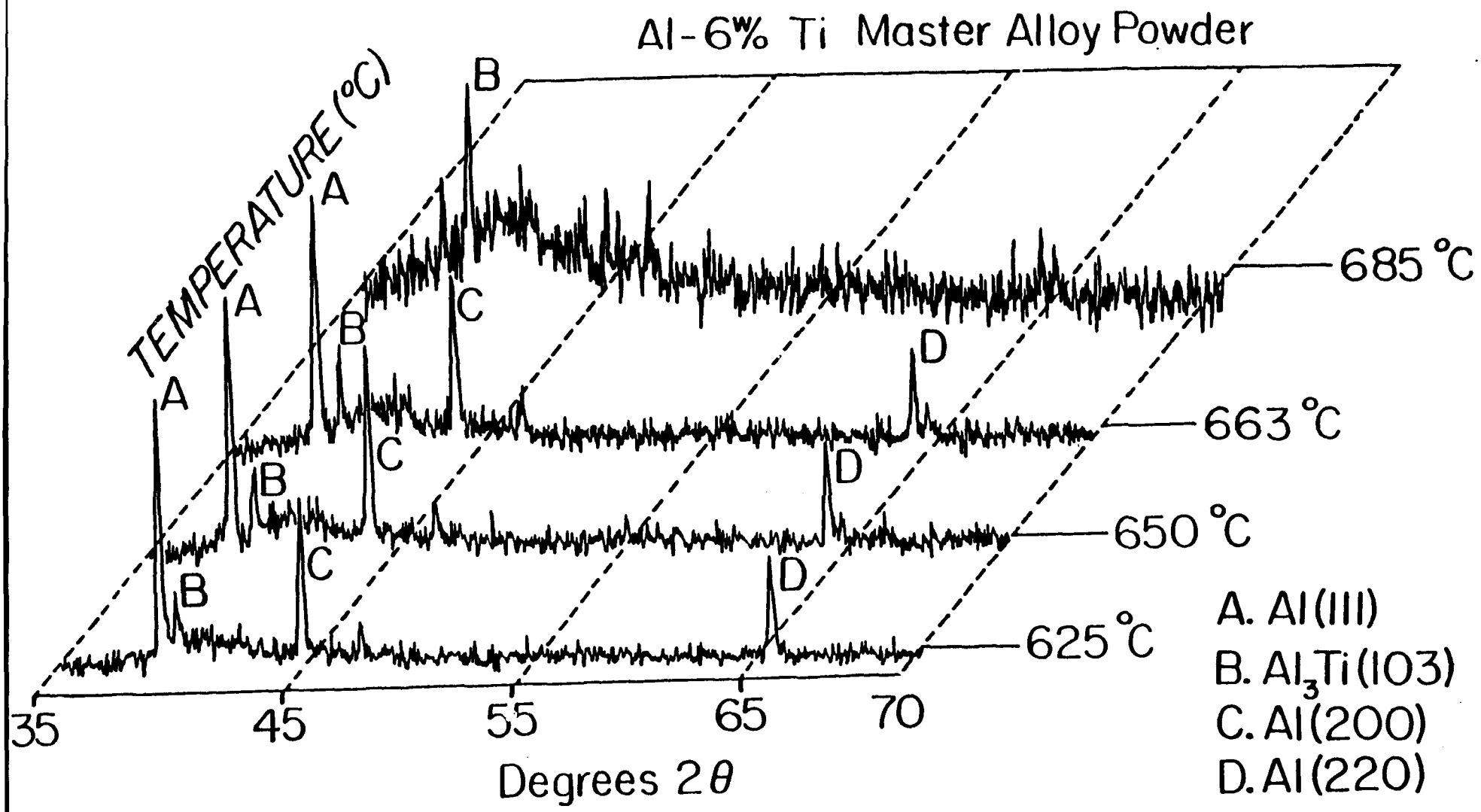

Figure 28. X-ray diffraction produced from scans of a Al-6wt% Ti grain refining master alloy powder sample at various temperatures below and above the equilibrium peritectic reaction which occurs at 665° C.